Curvature defects in a lamellar phase revealed by nuclear-spin-relaxation anisotropy

Per-Ola Quist and Bertil Halle
Condensed Matter Magnetic Resonance Group, Chemical Center, University of Lund, P.O. Box 124, S-221 00 Lund, Sweden
(Received 7 December 1992)

An aligned sample in the lamellar phase of the sodium dodecylsulphate–decanol–water system is investigated by orientation-dependent ^{23}Na NMR spin-relaxation experiments and x-ray diffraction. A pronounced relaxation anisotropy is observed, implying a nonclassical microstructure where a large fraction of the hydrocarbon-water interface is highly curved. Noting that the bilayer topology is either oil-continuous, bicontinuous, or water-continuous, we consider three classes of microstructures with curvature defects: a bilayer perforated by aqueous pores, a bilayer with aqueous slits and ribbonlike aggregates, and a bilayer fragmented into discrete discoidal micelles. The seven model-independent NMR observables impose severe constraints on the allowed microstructures: the discoid geometry can be rejected, while the pore and ribbon geometries are consistent with the data, but only for certain values of the relative defect dimensions. A simple analysis of the energetics of defect formation, using the deduced defect dimensions, favors the ribbon geometry.

PACS number(s): 61.30.Eb

I. INTRODUCTION

The lyotropic mesomorphism of amphiphile-water mixtures has been extensively studied over the past 50 years [1–3]. With increasing amphiphile concentration most systems exhibit the hexagonal→cubic→lamellar phase progression, sometimes with additional ("intermediate") phases occurring in the narrow concentration intervals separating the three classical phases. Until recently it was widely believed that the microstructure of a given phase, i.e., the geometry of the dividing interface that separates polar and nonpolar regions, is essentially invariant to changes in external conditions (temperature, composition) throughout the existence region of the phase. During the past decade, however, this traditional belief has been challenged by new experimental results, implying a continuous variation of microstructure. Near the phase boundaries these microstructural variations can be dramatic, involving changes in local symmetry and topology. Such modifications of the classical microstructure are commonly referred to as structural defects or, in the lamellar phase, curvature defects. In contrast to metastable textural defects [4,5], such as focal conic domains in the lamellar phase, the structural defect is an intrinsic feature of the equilibrium microstructure.

Most of the evidence for structural defects comes from studies of oriented lamellar (L_α) phases [6–40], mainly by small-angle x-ray and neutron scattering, conductivity, self-diffusion, and NMR spectroscopy. Among the investigated half-dozen different amphiphile-water systems, the perfluoro-octanoate (PFO)–water system (usually with cesium as counterion) is the earliest and most extensively studied [6–24]. For this system there is unambiguous evidence of structural defects in the L_α phase and for a continuous variation of the microstructure across the (second-order) transition to the neighboring discotic nematic (N_D) phase. While it is clear that the smectic amphiphile layers contain a substantial amount of water, the nature of the defects remains controversial. Similar results have been obtained for the decylammonium chloride–water–ammonium-chloride system [25–31], which also features an L_α phase next to an N_D phase. Structural defects in L_α phases have also been observed near the tetragonal phase in the sodium dodecylsulphate (SDS)–water [32,33] and LiPFO-water [8,17] systems, near the rectangular phase in the sodium decylsulphate–water–decanol system [34,35], near the isotropic microemulsion phase in the SDS–water–hexane–pentanol system [36] and near the microemulsion [37–39] and cubic [40] phases in the nonionic systems $C_{12}EO_n$ ($n=5$ or 6)–water ($C_{12}EO_n$ stands for n-ethyleneglycol dodecylether).

The quantitative characterization of structural defects in L_α phases poses challenging experimental problems. While there is ample *qualitative* evidence for the existence of defects, there is a striking lack of firm *quantitative* results on the geometry and density of defects.

Scattering techniques provide a correlation length (associated with the lateral diffuse scattering), which is a measure of defect density. (If the defects are ordered, the symmetry of the local "lattice" can also be deduced.) Information about the size and shape of the defects, however, can only be derived indirectly in terms of a specific geometric model.

Techniques that measure transport properties, such as conductivity and self-diffusion, are valuable as they reflect the topology of the microstructure, i.e., whether the bilayers are permeable to water and ions, and whether they are oil-continuous. To proceed beyond this qualitative topological information and make quantitative deductions about defect size, shape, and density requires a geometric model and a detailed analysis accounting for the dynamic consequences of microscopic interactions.

The two most popular models of structural defects in L_α phases are (i) a bilayer perforated by aqueous pores, and (ii) discoidal micelles with smectic translational or-

der. Neither scattering nor conductivity data can readily distinguish between these alternatives. (Self-diffusion of species solubilized in the nonpolar environment can in principle establish whether the bilayer plane is oil-continuous [20,30].)

Unlike these techniques, NMR [as well as electron-spin resonance (ESR)] probes the *curvature* of the interface, provided that the observed spin resides in a molecule that is effectively confined to the interface. Since the classical bilayer has zero curvature, a curvature-probing technique such as NMR should be useful for identifying and characterizing structural defects in L_α phases. The orientational correlations that carry the curvature information are manifested in the static line shape (and the line splitting derived therefrom) as well as in the spin-relaxation behavior. So far, only static line splittings in NMR [9,13,14,16,19,22,23,26,28,35,40] and ESR [36–38] have been used to study structural defects in L_α phases. To extract information about structural defects from such splittings, however, one requires a defect-free reference sample in which the local properties of the interface are the same as in the sample with defects. Even if this requirement could be met, the splitting cannot distinguish between intrinsic structural defects and larger-scale textural defects. Furthermore, only a single defect-related quantity is obtained, which obviously does not suffice to determine the size, shape, and density of defects.

In this work we introduce an alternative experimental approach to the problem of structural defects in L_α phases. We have previously used quadrupolar relaxation of interfacially confined nuclei (^{23}Na in the counterion and ^{2}H in the α-deuterated surfactant) to determine microstructure and interface dynamics in hexagonal [41–43] and nematic [44,45] phases. For a classical L_α phase, with planar interfaces, the spin relaxation is essentially determined by the local properties of the interface. Structural defects, by introducing interface curvature, qualitatively alter the spin-relaxation behavior: the lab-frame spectral densities (which are linearly related to the spin-relaxation rates) now depend on the frequency as well as on the orientation of the (macroscopically aligned) L_α phase. The orientation dependence, whose functional form is dictated by the point-group symmetry of the phase [46], provides the key to the fundamental relaxation observables: the crystal-frame spectral densities.

Crudely speaking, each of the three (in an L_α phase) crystal-frame spectral densities involves an amplitude factor and a correlation time [47]. The amplitude factors are determined by the distribution of local interface normals in the phase and, hence, reflect the interface curvature. Whereas the amplitude factors are invariant under isometric scaling of the microstructure, the dimensions of the structural defects can be deduced from the correlation times if the surface diffusion coefficient of the spin-bearing species is known.

We report here the results and analysis of a ^{23}Na spin-relaxation study of the counterions in the L_α phase of the system sodium dodecylsulphate–decanol–water at a composition close to the previously studied [44,45] discotic nematic phase. Four independent relaxation rates are determined at six different orientations of the macroscopically aligned L_α phase. This allows us to determine accurately the complete information content (nine crystal-frame spectral density values) of a fixed-field spin-relaxation study of an L_α phase. The observed strong frequency and orientation dependence constitute unambiguous evidence for a nonclassical microstructure with a large fraction curved interface.

In order to quantitatively characterize the structural defects we consider three topologically distinct types of microstructure: (i) a bilayer perforated by pores, (ii) a bilayer with line defects, giving rise to ribbonlike aggregates, and (iii) a bilayer fragmented into discrete discoidal aggregates. A quantitative analysis shows that the crystal-frame spectral densities are consistent with the first two types of defect, but only for certain values of the relative defect dimensions. To discriminate among these alternatives, we present a simple analysis of the energetics of defect formation, showing that the ribbon geometry is the most stable one.

II. EXPERIMENT

A. Materials and phase alignment

SDS (sodium dodecylsulphate) and *n*-decanol were obtained from BDH Chemicals ("specially pure" grade). The water was millipore-filtered H_2O with 10% D_2O added to allow the phase alignment to be monitored via the water ^{2}H NMR spectrum. All ^{23}Na NMR experiments were performed at 25.0 °C on a sample in the lamellar (L_α) phase of composition 27.30:7.00:65.70 wt. % SDS:decanol:water, corresponding to molar ratios $n_w/n_{\rm SDS}=38.12$ and $n_{\rm dec}/n_{\rm SDS}=0.467$. The L_α powder sample, prepared as in Ref. [42], showed birefringence between crossed polarizers but was distinctly more fluid than typical L_α samples. After exposure to an 8.5-T magnetic field for several hours, the water ^{2}H spectrum showed no signs of alignment.

At the present composition, the L_α phase is stable from 17 °C (where SDS precipitates) to 31 °C. In the range 32–34 °C, the L_α phase is in equilibrium with a discotic nematic (N_D) phase, and in the range 36–40 °C with an isotropic micellar phase. Figure 1 shows the relevant part of the ternary phase diagram at 25 °C.

Two methods are available for preparing macroscopically aligned L_α phases: surface-induced alignment between stacked glass plates, and magnetic-torque alignment during a temperature-induced phase transition from an isotropic or nematic phase. A drawback of the first method is the small plate spacing (~ 50 μm) required to get a good alignment; the large fraction glass in the sample reduces considerably the signal-to-noise ratio. The main drawback of the second method is that it does not produce a uniform alignment of the hydrocarbon bilayers, but rather a distribution of director orientations in the plane perpendicular to the magnetic field. In the present study, these drawbacks were largely avoided by combining the two methods.

The sample cell used for the relaxation anisotropy measurements is shown in Fig. 2: 18 glass plates of 20-mm

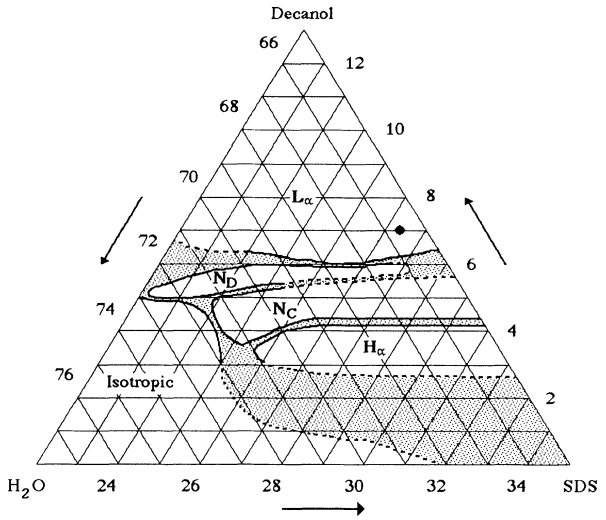

FIG. 1. Partial phase diagram (wt. %) for the system SDS-decanol-water (10% D_2O in H_2O) at 25 °C showing the extension of the one-phase regions of the isotropic micellar solution phase and the lamellar (L_α), hexagonal (H_α), and nematic (N_C,N_D) liquid-crystalline phases. (The dashed boundaries have not been precisely located.) The dot in the L_α phase corresponds to the composition of the investigated sample.

height and 120-μm thickness were fixed between two cylindrical plastic (Kel-F) spacer plugs (with 150-μm-wide slots every 450 μm), yielding a cylindrical glass lattice of ~9-mm diam, 15-mm height, and ~330 μm between the glass plates. The lattice was placed in a 50-mm-long, 10-mm NMR tube, the L_α phase was introduced by slow centrifugation, and the sample was sealed with a Teflon-coated, cylindrical rubber plug and Parafilm. No signs of material loss were detected during the relaxation experiments.

For the alignment, the sample was placed with an 8.5-T magnetic field along the sample tube axis. At this stage, the water ^2H spectrum resembled a typical three-

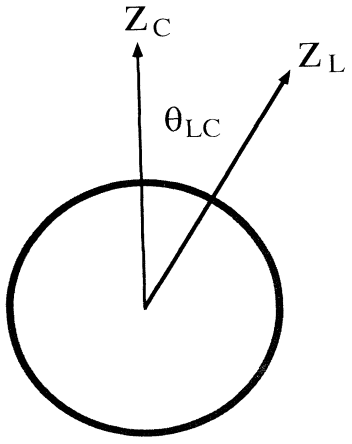

FIG. 2. Cross section of the sample cell used for the relaxation anisotropy measurements. The orientation θ_{LC} between the phase director (z_C) and the magnetic field (z_L) was varied by twisting the cylindrical sample tube around its axis.

dimensional powder spectrum of a uniaxial phase [48]. By raising the temperature to the two-phase region, with the L_α phase in equilibrium with the isotropic micellar phase, for ~5 min and then quickly cooling back to 25 °C, a uniformly aligned L_α phase was obtained. The water ^2H spectrum showed two peaks with a splitting identical to the previous powder splitting. After a 90° rotation of the sample (to $\theta_{LC}=0°$ in Fig. 2) the water ^2H spectrum was dominated by two peaks with a splitting twice as large as the powder splitting. A small (two-dimensional) powderlike signal was also seen, which we attribute to the small fraction of the L_α phase that aligns on the NMR tube. From the geometry of the sample cell, we estimate that at least 85–90 % of the L_α phase is uniformly aligned.

B. X-ray diffraction

An x-ray-diffraction experiment was performed on a powder sample at 25 °C. The Bragg reflections were recorded directly on film in a Kiessig camera, using monochromatic Cu $K\alpha$ radiation ($\lambda=1.54$ Å). The diffraction pattern clearly revealed two lines with Bragg spacings of 58.4 and 29.4 Å, in agreement with the theoretical prediction 1:1/2 for an L_α phase [1]. Averaging the two values, we thus obtain a smectic repeat distance of $d=58.6$ Å.

C. ^{23}Na spin relaxation

The ^{23}Na experiments were performed on a Bruker MSL-100 spectrometer (^{23}Na resonance frequency, 26.487 MHz) with a horizontal 10-mm solenoidal probe and a 2.35-T-wide-bore superconducting magnet. The magnetic field inhomogeneity was 10–20 Hz (cf. below) and the temperature stability and gradients in the sample were less than ±0.04 °C. Typically the 180° pulse length was 12 μs. All experiments were performed on resonance, i.e., the rf pulse was centered on the central peak frequency.

The orientation of the phase director was varied by simply twisting the sample tube around its axis (Fig. 2). Since the phase is uniaxial and the ^{23}Na satellites narrow (Fig. 3), the crystal orientation θ_{LC} was first estimated by eye to within ±5° or so and then more precisely determined from the known angular dependence of the quadrupole splitting [48]

$$\nu_Q(\theta_{LC})=\nu_Q^{90}(3\cos^2\theta_{LC}-1)\ , \tag{2.1}$$

with the 90° splitting ν_Q^{90} determined from a spectrum with the sample in a vertical probe (with the phase director uniformly perpendicular to the magnetic field). The reference splitting obtained in this way, $|\nu_Q^{90}|=16.14$ kHz, agreed well with the 90° and 0° splittings derived from the singularities of the small powderlike fraction in the sample (Fig. 3). From the uncertainty in the splitting, we estimate the uncertainty in the crystal orientation θ_{LC} to be ±1° or less. In the relaxation anisotropy experiments θ_{LC} was varied nonmonotonically in order to detect (and minimize systematic errors due to) any slow time-dependent changes in the sample (e.g., due to eva-

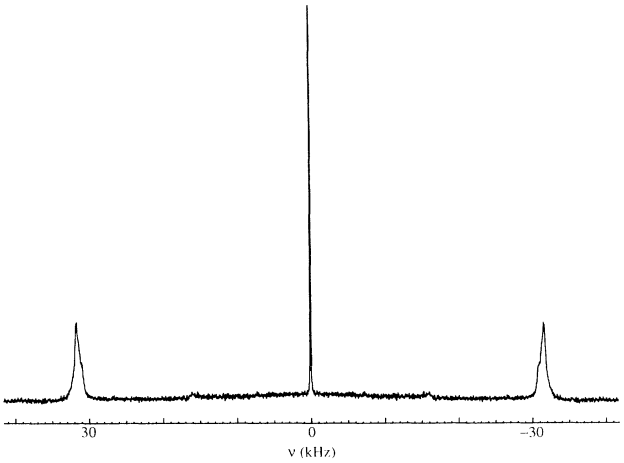

FIG. 3. ^{23}Na NMR $F2$ spectrum obtained from shortest t_1 delay in a 2DQE experiment at $\theta_{LC}=6.8°$. The central peak is truncated at $\frac{1}{3}$ of its actual height.

poration). However, no such changes were detected.

The two nonadiabatic (high-frequency) lab-frame spectral densities $J^L_{11}(\omega_L,\theta_{LC})$ and $J^L_{22}(2\omega_L,\theta_{LC})$ were determined from three independent relaxation experiments. Redundancy was needed to accurately determine the, sometimes very similar, spectral densities. Due to the small powderlike fraction in the sample, the central peak is expected to show multiexponential relaxation and can therefore not be used for accurate spectral density determinations. Instead, $J^L_{11}(\omega_L,\theta_{LC})$ and $J^L_{22}(2\omega_L,\theta_{LC})$ were determined from the ^{23}Na satellites, using the following three relaxation experiments. These particular experiments were chosen to optimize the accuracy of the determined spectral densities for a given measurement time [93].

Conventional inversion recovery (IR), $(180°)_\phi$-τ-$(90°)_x$-acquisition (acq.), yielding a single-exponential recovery of the satellite intensity according to [49]

$$I_{\mathrm{IR90}}(\tau)=a+b\exp[-2J^L_2\tau]\ . \tag{2.2}$$

For convenience, the lab-frame spectral densities $J^L_k\equiv J^L_{kk}(k\omega_L,\theta_{LC})$ are defined so as to include spin-dependent numerical factors and coupling constants.

Modified inversion recovery, $(180°)_\phi$-τ-$(35°)_x$-acq., performed as the conventional experiment except for the detection pulse angle, yielding a biexponential satellite recovery with maximized amplitude for the exponential involving J^L_1 [49],

$$I_{\mathrm{IR35}}(\tau)=c+d\exp[-2J^L_1\tau]+f\exp[-2J^L_2\tau]\ . \tag{2.3}$$

Quadrupole polarization decay (QPD), using the Jeener-Broekaert pulse sequence $(90°)_\phi$-τ_1-$(45°)_{\phi\pm\pi/2}$-τ-$(45°)_x$-$(\pm)$acq., yielding an exponential decay of the satellite intensities according to [49]

$$I_{\mathrm{QPD}}(\tau)=g+h\exp[-2(J^L_1+J^L_2)\tau]\ . \tag{2.4}$$

The fixed delay time τ_1 was set to $1/(4\nu_Q)$ in order to maximize the conversion from dipolar to quadrupolar polarization [49].

In all three experiments the acquisition delay was set to a multiple of $1/\nu_Q(\theta_{LC})$ in order to avoid baseline offsets due to first-order phase corrections. The experiments were performed with 24 different delay times τ in the range 0.5–140 ms for the inversion recoveries and 0.25–70 ms for the quadrupole polarization decay. A rms satellite peak signal-to-noise ratio of better than 100 was obtained in each experiment with the shortest delay time. The repetition time between successive accumulations was 140 ms or longer.

A simultaneous least-squares fit [50] of (2.2)–(2.4) to the $2\times3\times24$ intensities I_{IR90}, I_{IR35}, and I_{QPD} yielded the nine parameters $J^L_1,J^L_2,a,b,\ldots,g$ at each crystal orientation θ_{LC}. In all fits the computed rms intensity uncertainty was close to the inverse of the experimental rms signal-to-noise ratio. The amplitude parameters a–g were close to their relative theoretical values [49], except at the largest quadrupole splittings where the 180° pulse was not perfectly nonselective (cf. below), causing the b, d, and f coefficients to deviate (by up to 25%) from their nominal (hard-pulse) values [93]. The deduced lab-frame spectral densities J^L_1 and J^L_2, the splitting ν_Q, and the inhomogeneous central ($\Delta\nu^c_{\mathrm{inh}}$) and satellite ($\Delta\nu^s_{\mathrm{inh}}$) linewidths at half-height are collected in Table I. The central line always had a Lorentzian shape, whereas the satellite line shape was a superposition of homogeneous Lorentzian shapes, as expected for a small spread ($\sim\pm2°$) in the crystal orientation (Fig. 3). This spread is presumably caused by a variation in the orientation of the glass plates. No variation in the relaxation rates was observed at different positions within the satellite peak.

The rf pulses used in the quadrupole polarization experiment to determine the sum $J^L_1+J^L_2$ showed less than 6% attenuation at the satellite positions and, hence, can be considered nonselective. However, for the 180° pulses

TABLE I. Orientation dependence of quadrupole splitting, inhomogeneous linewidths, and nonadiabatic laboratory-frame spectral densities for ^{23}Na in the L_α phase. The experimental random error ($\pm2\sigma$) is given for the spectral densities. The random error is estimated to be ±5 Hz in ν_Q and $\Delta\nu^c_{\mathrm{inh}}$, and $\pm5\%$ in $\Delta\nu^s_{\mathrm{inh}}$.

$\lvert\nu_Q\rvert$ (kHz)	θ_{LC} (deg)	$\Delta\nu^c_{\mathrm{inh}}$ (Hz)	$\Delta\nu^s_{\mathrm{inh}}$ (Hz)	J^L_1 (s^{-1})	J^L_2 (s^{-1})
32.03	4.1	50	390	46.2±1.3	28.3±0.4
26.79	19.7	46	500	48.8±1.2	29.1±0.3
12.64	39.6	46	740	51.8±1.0	33.8±0.2
4.23	60.3	45	370	45.6±1.6	40.2±0.4
12.64	74.4	46	420	41.0±1.8	44.0±0.5
16.06	87.7	45	190	39.1±1.8	46.0±0.6

TABLE II. Orientation dependence of quadrupole splitting, 2DQE linewidths, and adiabatic laboratory-frame spectral density for ^{23}Na in the L_α phase. The experimental random error ($\pm 2\sigma$) is 7% for J_0^L. The random error is estimated to be ± 5 Hz in ν_Q, ± 1 Hz in $\Delta\nu_{QE}^c$, and ± 3 Hz in $\Delta\nu_{QE}^s$.

$\lvert\nu_Q\rvert$ (kHz)	θ_{LC} (deg)	$\Delta\nu_{QE}^c$ (Hz)	$\Delta\nu_{QE}^s$ (Hz)	J_0^L (s^{-1})
31.60	6.8	26.4	88.5	195
27.55	18.2	29.3	91.8	196
14.04	37.9	30.1	107	242
4.64	60.8	31.3	84.3	166
15.60	83.9	30.0	61.7	99.5

used in the inversion recovery experiments to separately determine J_1^L and J_2^L, the attenuation is $\sim 20\%$ for the largest quadrupole splitting. This imperfect pulse nonselectivity effects the values of the coefficients in (2.2) and (2.3), but does not affect the exponents [93]. Consequently, the effect on the crystal-frame spectral densities derived from the orientation dependence of J_1^L and J_2^L (Sec. III) should be negligible; indeed, omission of the data from the two smallest angles θ_{LC} (with the largest splittings) does not significantly affect the fitted crystal-frame spectral densities.

In a second experimental series, the adiabatic (zero-frequency) lab-frame spectral density $J_0^L \equiv J_{00}^L(0,\theta_{LC})$ was determined by a *two-dimensional quadrupolar echo* (2DQE), $(90°)_x$-τ-$(90°)\pm_y$-τ-acq., as described elsewhere [41,51]. Figure 3 shows a ^{23}Na $F2$ spectrum recorded during the 2DQE experiment. (The $F2$ spectrum is the Fourier transform of the signal recorded in the acquisition period t_2. The $F1$ spectrum is the Fourier transform with respect to the refocusing time τ of one of the $F2$ peaks.) The magnetic-field inhomogeneity in the 2DQE experiment was estimated to be $\delta \approx 10$ Hz. From the difference in linewidth at half-height of the central line in the $F1$ spectra derived from the $F2$ central peak ($\Delta\nu_{QE}^c$) and from the $F2$ satellite peak ($\Delta\nu_{QE}^s$), we determine J_0^L according to [41,51]

$$J_0^L = \pi(\Delta\nu_{QE}^s - \Delta\nu_{QE}^c) \ . \tag{2.5}$$

$\Delta\nu_{QE}^c$ and $\Delta\nu_{QE}^s$ were determined from Lorentzian fits to the central peak. This procedure introduces a small systematic error in J_0^L, since the central peak in $F2$ contains contributions from all crystal orientations present in the sample, i.e., also from the small powder fraction. We believe, however, that this error is negligible since (i) $\Delta\nu_{QE}^c \ll \Delta\nu_{QE}^s$, (ii) the aligned powder fraction is small, and (iii) the angular dependence of $\Delta\nu_{QE}^c$ ($\approx J_1^L + J_2^L + \delta/2$) is weak (cf. Table I). The results of the 2DQE experiments are collected in Table II.

III. SPIN-RELAXATION ANISOTROPY

The lab-frame spectral densities $J_{kk}^L(k\omega_L,\theta_{LC})$, determined from the spin-relaxation experiments described in Sec. II C, depend on the orientation, θ_{LC}, of the aligned liquid crystal with respect to the static magnetic field (Tables I and II). The functional form of this orientation dependence is completely determined by the macroscopic

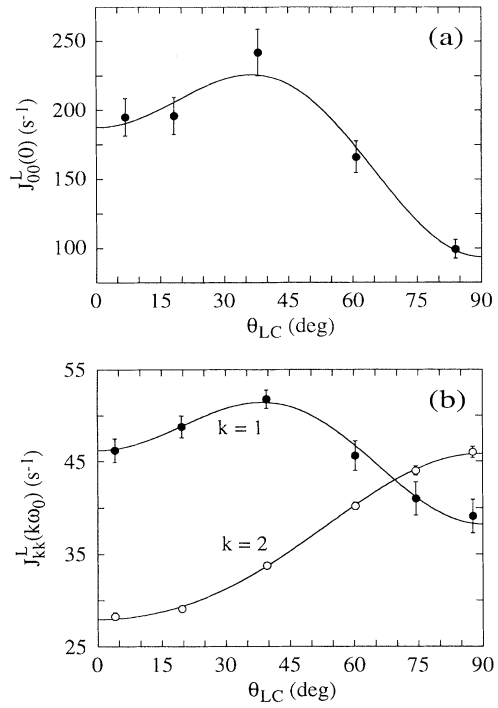

FIG. 4. Orientation dependence of the adiabatic (a) and nonadiabatic (b) laboratory-frame spectral densities. The curves resulted from fits of Eqs. (3.1) and (3.2), with the nine crystal-frame spectral densities given in Table III.

orientational symmetry (point group) of the mesophase [46]. For a uniaxial phase, such as L_α (point group $D_{\infty h}$), the orientation dependence takes the form [52–54]

$$J_{kk}^L(k\omega_L,\theta_{LC}) = \sum_{n=0}^{2} F_{kn}(\theta_{LC}) J_{nn}^C(k\omega_L) \ . \tag{3.1}$$

The angular functions $F_{kn}(\theta_{LC})$ can be expressed in terms of the reduced Wigner functions [55] $d_{kn}^2(\theta_{LC})$ as

$$F_{kn}(\theta_{LC}) = (1-\delta_{n0}/2)\{[d_{kn}^2(\theta_{LC})]^2 + [d_{k-n}^2(\theta_{LC})]^2\} \ . \tag{3.2}$$

The uniaxial relaxation anisotropy in (3.1) applies to any phase which has an effectively uniaxial symmetry with respect to a fourth-rank tensor [46,47]. In practice, this means point-group symmetry D_6 or higher. Although the macroscopic symmetry of an L_α phase is $D_{\infty h}$, the *local* symmetry may be lower in the presence of structural defects. Even if the local symmetry is lower

TABLE III. Crystal-frame spectral densities for ^{23}Na in the L_α phase. The propagated experimental random error ($\pm 2\sigma$) is given.

	$J_{nn}^C(k\omega_L)$ (s^{-1})		
k	$n=0$	$n=1$	$n=2$
0	187±12	261±17	63±10
1	74.9±3.8	46.2±1.1	30.3±2.8
2	60.1±2.3	39.6±1.3	28.0±0.3

than D_6, however, the uniaxial form (3.1) remains valid provided that the observed nucleus samples the global ($D_{\infty h}$) symmetry on a time scale that is long compared to the variation in the local spin-relaxation rates (which would be observable in the absence of such fast sampling). This point is further discussed in Secs. VI A and VII A.

The set of nine crystal-frame spectral densities (CFSD's), $J^C_{nn}(k\omega_L)$ with k, $n=0,1,2$, constitutes the complete, model-independent information content accessible by fixed-field spin-relaxation measurements on a uniaxial phase. Using (3.1) and (3.2) we determine the nine CFSD's by generalized linear least-squares fits [50] to the lab-frame spectral densities in Tables I and II. The fits are shown in Fig. 4 and the resulting CFSD's are collected in Table III.

IV. EVIDENCE FOR CURVATURE DEFECTS

The CFSD's in Table III reflect thermal fluctuations in the components of the electric-field gradient (EFG) tensor at the Na^+ nucleus. In a classical lamellar phase, built from homogeneous *planar* bilayers, only two kinds of motion contribute to the EFG fluctuations: fast local motions and counterion diffusion along the bilayer normal.

The local motions comprise restricted motions (librations and intermolecular vibrations) within the primary hydration "shell" of the counterion (time scale 10^{-13} s), collective hydration dynamics (10^{-12} s), and local (length scale 10^{-10} m) counterion and surfactant headgroup motions (10^{-12}–10^{-10} s) [56–58]. At conventional magnetic fields these motions are much faster than the Larmor frequency ω_L (here $1/\omega_L=6.0$ ns), and thus contribute equally to the adiabatic and nonadiabatic spectral densities. The observation of a quadrupole splitting implies that the local motions experience orientational restrictions (imposed by the charged bilayer surfaces). However, since the local quadrupole coupling constant (QCC) ($\chi_{\rm loc}\approx 100$ kHz [42,43]) is roughly a factor 40 smaller than the rms QCC [58], the effect of local anisotropy on the fast-motion spectral densities is negligible. Consequently, the local motions merely add a constant contribution $J_{\rm loc}\equiv J^{C,{\rm loc}}_{nn}(0)$ to all nine CFSD's. In a recent study [43] of the ^{23}Na relaxation anisotropy in the H_α phase of the present system, we demonstrated explicitly that $J_{\rm loc}$ is indeed independent of k (extreme narrowing) and n (weak anisotropy).

The local motions establish a locally averaged EFG tensor and a corresponding local QCC $\chi_{\rm loc}$. As a result of counterion diffusion relative to the bilayer surface, $\chi_{\rm loc}$ fluctuates in magnitude, thereby inducing spin relaxation. In a classical lamellar phase only counterion diffusion along the bilayer normal causes $\chi_{\rm loc}$ to fluctuate and, since the local EFG is uniaxial, contributes only to the three CFSD's with symmetry index $n=0$ [59]. In Appendix A we show, through explicit calculations for a realistic model, that "radial" (along the bilayer normal) counterion diffusion contributes with a small ($<10\ {\rm s}^{-1}$) constant (extreme narrowing) term $J^C_{\rm rad}\equiv J^{C,{\rm rad}}_{00}(0)$ to each of the three CFSD's $J^C_{00}(k\omega_L)$.

For a classical L_α phase, with homogeneous planar bilayers, the CFSD's thus take the form

$$J^C_{nn}(k\omega_L)=J_{\rm loc}+\delta_{n0}J^C_{\rm rad}\ , \tag{4.1}$$

with $J^C_{\rm rad}<10\ {\rm s}^{-1}$. It is abundantly clear that (4.1) does not even qualitatively describe the data in Table III. We thus conclude that, in the investigated sample, *the bilayers are not homogeneous and planar.*

As in all liquid crystals, the microstructure of the L_α phase is subject to thermal fluctuations. Of particular importance for the NMR behavior are those fluctuation modes that introduce bilayer curvature, i.e., the smectic undulation modes [60–62]. In the present L_α phase, with densely spaced and highly charged bilayers (without neutral salt), the dominant undulation modes are expected to be of small amplitude and of long wavelength [63,64]. In the case of counterion spin relaxation, we therefore expect contributions from counterion diffusion along the undulating bilayer only to the adiabatic spectral densities [45]. If bilayer undulations were to contribute to the nonadiabatic spectral densities, they would mainly affect $J^C_{11}(k\omega_L)$, which is of second order in the fluctuation amplitude while $J^C_{00}(k\omega_L)$ and $J^C_{22}(k\omega_L)$ are of fourth order [45]. However, in our recent ^{23}Na spin-relaxation study of the H_α phase, such nonadiabatic contributions were shown to be negligible [43].

Taking bilayer undulations into account, the CFSD's for a classical L_α phase should thus be of the form

$$J^C_{nn}(k\omega_L)=J_{\rm loc}+\delta_{n0}J^C_{\rm rad}+\delta_{k0}J^{C,{\rm und}}_{nn}(0)\ . \tag{4.2}$$

As seen from Table III, however, the nonadiabatic CFSD's exhibit a considerable frequency dependence and depend strongly on the symmetry index n. Since these features can only be accounted for by counterion diffusion over a highly curved bilayer surface, we conclude that *the bilayers contain intrinsic structural defects.* The frequency dependence provides a rough estimate of the length scale L of these defects, since the characteristic diffusion time $L^2/(4D_s)$ must be of the order of the Larmor period $1/\omega_L=6.0$ ns. With the surface diffusion coefficient $D_s=4.4\times10^{-10}\ {\rm m}^2\,{\rm s}^{-1}$, as determined for the Na^+ counterions in the H_α phase [42,43], we thus find $L\approx 30$ Å, comparable to the bilayer thickness.

As we are concerned here with the "ground-state" microstructure of the L_α phase, we consider henceforth only the six nonadiabatic CFSD's. Dropping the undulation contribution in (4.2) and introducing a contribution from counterion diffusion over the curved surface of the defects, we have

$$J^C_{nn}(k\omega_L)=J_{\rm loc}+\delta_{n0}J^C_{\rm rad}+J^{C,{\rm def}}_{nn}(k\omega_L)\ . \tag{4.3}$$

The validity of this formal decomposition of the CFSD's is ensured by the time-scale separation of the dynamic processes responsible for each of the three terms [47]. [The time scale of the radial contribution (Appendix A) is an order of magnitude shorter than the characteristic time for counterion diffusion over the bilayer defects (cf. above).]

The defect spectral densities in (4.3) can be expressed (for a spin $I=\frac{3}{2}$ nucleus) as

$$J_{nn}^{C,\mathrm{def}}(k\omega_L)=\pi^2\bar{\chi}^2 A_n j_{nn}^{\mathrm{def}}(k\omega_L)\ , \tag{4.4}$$

where $\bar{\chi}$ is the residual QCC, which is spatially averaged by counterion diffusion along the bilayer normal and hence equal to $P\chi_{\mathrm{loc}}$ (Appendix A). The reduced spectral densities (with the dimensions of time), associated with counterion diffusion over the defects, are defined in terms of Wigner functions [55] as

$$j_{nn}^{\mathrm{def}}(k\omega_L)=\frac{1}{A_n}\int_0^\infty dt\,\cos(k\omega_L t) \times[\,\langle D_{n0}^{2*}(\Omega_{CN}^0)D_{n0}^2(\Omega_{CN})\rangle-\delta_{n0}A_Q^2\,], \tag{4.5}$$

where $\Omega_{CN}=(\phi_C,\theta_{CN},-)$ are the time-dependent Euler angles specifying the transformation from the crystal frame C (z_C=symmetry axis of the L_α phase) to the interface frame N (z_N=local surface normal). (We assume here that $\bar{\chi}$ is laterally uniform.) The three fluctuation amplitudes A_n are simply the initial values of the time correlation functions within square brackets in (4.5), i.e.,

$$A_n=\langle[d_{n0}^2(\theta_{CN})]^2\rangle-\delta_{n0}A_Q^2\ , \tag{4.6}$$

with

$$A_Q=\langle d_{00}^2(\theta_{CN})\rangle\ . \tag{4.7}$$

To quantitatively characterize the bilayer defects we must introduce a geometric model that allows us to express the fluctuation amplitudes in (4.6) and the reduced spectral densities in (4.5) in terms of the parameters describing the defect shape and density, and the counterion surface diffusion coefficient. This is the subject of Secs. V–VIII. Already at this stage, however, we can exclude the class of defect models that only introduces surfaces perpendicular to the smectic plane, e.g., straight cylindrical pores or rectangular slits. For this class of defect models, with $\theta_{CN}=\pi/2$, the quantity within square brackets in (4.5) vanishes identically for $n=0$ and 1. Surface diffusion over defects can then contribute only to $J_{22}^C(k\omega_L)$, in striking disagreement with the experimental results in Table III.

In the following analysis we set $J_{\mathrm{rad}}^C=0$ in (4.3). As discussed in Appendix A and Sec. X, the conclusions regarding bilayer defects are only marginally affected by allowing for an estimated contribution of $J_{\mathrm{rad}}^C<10\ \mathrm{s}^{-1}$ from "radial" counterion diffusion.

The quadrupole splitting ν_Q is a valuable complement to the spectral density data since it involves the residual QCC $\bar{\chi}$ and the geometric parameter A_Q, which also appear in the spectral densities $J_{nn}^{C,\mathrm{def}}(k\omega_L)$. Since the undulation modes are expected to be of small amplitude (cf. above), we neglect their effect on the quadrupole splitting, which then takes the form (for a spin $I=\frac{3}{2}$ nucleus)

$$\nu_Q^0\equiv\nu_Q(\theta_{LC}=0)=\tfrac{1}{2}A_Q\bar{\chi}\ . \tag{4.8}$$

In Sec. III, we tacitly neglected, for the same reason, the smoothing effect of bilayer undulations on the orientation dependence of the lab-frame spectral densities in (3.1).

V. DEFECT TOPOLOGY AND SYMMETRY

Having relinquished the notion of a classical bilayer, we now face the problem of quantitatively characterizing the unknown microstructure and of calculating the spectral density contributions $J_{nn}^{C,\mathrm{def}}(k\omega_L)$ associated with diffusion over the surface of this microstructure. Although we cannot expect to uniquely determine the microstructure, the six nonadiabatic CFSD's and the quadrupole splitting impose severe constraints on the allowed microstructures. These data can be analyzed in several ways.

One approach is to introduce a detailed geometric model for the microstructure and to fit the parameters in this model directly to the data. We shall take a more general approach, however, where the data analysis is performed in two steps. In the first step, we transform the data into quantities that are more directly amenable to physical interpretation in terms of microstructure and dynamics. The nature of this transformation depends on the *general* properties of the defects, notably their topology, point-group symmetry, and orientational order, but does *not* depend on the detailed geometry (dimensions and curvatures) of the defects. Given the general properties, this transformation is unique, i.e., it is a one-to-one mapping.

The transformed quantities include the local-motion contribution J_{loc}, the residual QCC $\bar{\chi}$, and the fluctuation amplitudes A_n. The latter are static quantities, independent of the surface diffusion dynamics, and can be given a geometrical meaning. They are model independent in the sense noted above, and can be related to results from other physical experiments or from computer simulations.

In the second step of the analysis, we provide explicit geometric interpretations of the fluctuation amplitudes (or of closely related quantities) in terms of several specific microstructural models. The geometric model parameters thus determined should be regarded as illustrations of how the model-independent quantities can be realized in terms of physically reasonable microstructures. It should be understood, however, that we cannot arrive at a unique microstructure; we can merely establish whether a given microstructure is *consistent* with the data.

Considering the microstructure of the nearby nematic and hexagonal phases (Fig. 1), we focus on microstructures for the L_α phase that introduce water into the bilayers in such a way that the average mean curvature of the monolayer is positive, i.e., convex towards water. We thus exclude "reversed defects," connecting adjacent bilayers. The topology of the oil and water regions *within the bilayer* admits three possibilities: the bilayer can be oil-continuous, bicontinuous, or water-continuous. This corresponds, respectively, to point defects (aqueous pores), line defects (aqueous slits or amphiphile ribbons), and reversed point defects (discrete micelles with smectic translational order).

For simplicity, and also on physical grounds, we impose certain symmetry constraints on the defects. The pores and micelles are taken to be uniaxial, by which we mean point-group symmetry D_{6h} or higher [46,47]. The

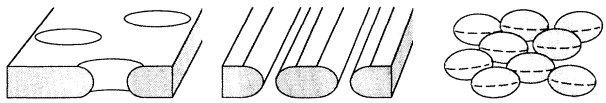

FIG. 5. The three topological types of structural defect that impart a positive average mean curvature to the bilayer interface.

symmetry axis of every pore is taken to be parallel to the bilayer normal and, neglecting bilayer undulations, to the symmetry axis of the L_α phase. The micelles, however, need not be perfectly aligned. On physical grounds, we expect the micelles to have a discoidal shape. The line defects can be viewed either as aqueous slits or as amphiphilic ribbons. They are taken to be of indefinite length (end effects are neglected) and locally of D_{2h} symmetry (with the two-fold axis in the bilayer plane). We shall refer to these three types of microstructure as pores, ribbons, and discoids. They are schematically illustrated in Fig. 5.

Since the bilayer is fluid, the defects must be dynamic entities: they are continuously created and annihilated. These processes are expected to be slow since they involve energetically unfavorable oil-water contact. On the time scale of counterion diffusion over the curved defect surface (a few nanoseconds), the defect geometry can thus be regarded as static. The dynamic nature of the defects also implies that they are polydisperse in size and shape. In the following analysis, however, we do not explicitly take defect polydispersity into account.

VI. PORES

A. Spectral densities

We consider now the contributions $J_{nn}^{C,\mathrm{def}}(k\omega_L)$ to the nonadiabatic CFSD's from counterion diffusion over the surface of a bilayer containing uniaxial pores (cf. Fig. 5). The decomposition of the lab-frame spectral densities in terms of three CFSD functions presupposes an effectively uniaxial symmetry of the entire surface on the time scale on which the corresponding time correlation functions decay (Sec. III). In principle, the inclusion of pores into the bilayer breaks the uniaxial symmetry of the latter (except in the special case of a hexagonal pore distribution). In practice, however, the deviation from uniaxial relaxation behavior is not likely to be significant, in particular, as regards the nonadiabatic CFSD's.

Rather than specifying the pore geometry at the outset, we assume that the reduced spectral densities in (4.5) are Lorentzian. Neglecting the radial contribution in (4.3) (cf. Sec. IV and Appendix A), we then obtain for the six nonadiabatic CFSD's

$$J_{nn}^{C}(k\omega_L)=J_{\mathrm{loc}}+\pi^2\bar{\chi}^2 A_n\frac{\tau_n}{1+(k\omega_L\tau_n)^2}\ , \tag{6.1}$$

where ω_L is the Larmor frequency and the τ_n are (effective) correlation times associated with diffusion over the curved surface. The accuracy of this Lorentzian approximation can be assessed for particular surface geometries where $J_{nn}^{C,\mathrm{def}}(k\omega_L)$ has been calculated exactly. This is the case for spherical and cylindrical surfaces, where (6.1) is exact, and for spheroidal [54] and catenoidal [65] surfaces, where the systematic error introduced by the Lorentzian approximation is smaller than the present random errors propagated from the experimental uncertainties (cf. below).

The three amplitude factors A_n, defined by (4.6), can be expressed in terms of two independent quantities [46,54], usually chosen as the second-rank and fourth-rank orientational order parameters $\langle P_2(\cos\theta_{CN})\rangle$ and $\langle P_4(\cos\theta_{CN})\rangle$. We can therefore, for example, express A_0 in terms of A_1 and A_2 as

$$A_0=6A_2-(A_1+4A_2)^2\ . \tag{6.2}$$

We choose as independent parameters the quantities σ_2 and σ_4, defined through

$$\sigma_m=\langle\sin^m\theta_{CN}\rangle=\int_0^\pi d\theta_{CN} f(\theta_{CN})\sin^m\theta_{CN}\ , \tag{6.3}$$

where $f(\theta_{CN})$ is the normalized distribution function for the local interface normal orientations experienced by the Na^+ counterions. The non-negative quantities σ_2 and σ_4 are convenient in the present context since they vanish for a classical (planar) bilayer. From (4.6) and (6.3) we obtain

$$A_0=\tfrac{9}{4}(\sigma_4-\sigma_2^2)\ , \tag{6.4a}$$

$$A_1=\tfrac{3}{2}(\sigma_2-\sigma_4)\ , \tag{6.4b}$$

$$A_2=\tfrac{3}{8}\sigma_4\ . \tag{6.4c}$$

The following general inequalities can be established for the amplitude factors:

$$0\le A_0\le\tfrac{9}{16},\quad 0\le A_1,A_2\le\tfrac{3}{8},\quad -\tfrac{1}{2}\le A_Q\le 1\ , \tag{6.5}$$

and for the parameters σ_2 and σ_4:

$$0\le\sigma_4\le\sigma_2\le\sqrt{\sigma_4}\le 1\ . \tag{6.6}$$

For a continuous bilayer with pore defects, the distribution function $f(\theta_{CN})$, and hence the parameters σ_2 and σ_4, depend on the geometry of the defects as well as on their density. These factors can be formally separated by writing

$$f(\theta_{CN})=x\hat{f}(\theta_{CN})+(1-x)\delta(\theta_{CN})\ , \tag{6.7}$$

where x is the fraction of the bilayer surface that belongs to defects and $\hat{f}(\theta_{CN})$ is the distribution function for a defect. Combination of (6.3) and (6.7) yields

$$\sigma_m=x\hat{\sigma}_m\ , \tag{6.8}$$

where $\hat{\sigma}_m$ refers to the defect. In contrast, the correlation times τ_n do not depend in a simple way on the defect area fraction x. The factorization in (6.8) shows that the ratio $\sigma_2/\sigma_4=\hat{\sigma}_2/\hat{\sigma}_4$ is an intrinsic property of the pore defect.

B. Data transformation

The six nonadiabatic CFSD's in (6.1) are determined by the seven independent quantities J_{loc}, $\bar{\chi}$, σ_2, σ_4, τ_0, τ_1,

TABLE IV. Quantities derived from the quadrupole splitting and the nonadiabatic CFSD's assuming uniaxial pores.

Quantity	Value
J_{loc} (s^{-1})	17±5
$\|\bar{\chi}\|$ (kHz)	111±8
σ_2	0.28±0.03
σ_4	0.19±0.02
σ_2/σ_4	1.48±0.06
τ_0 (ns)	2.2±0.4
τ_1 (ns)	2.0±0.4
τ_2 (ns)	1.7±0.7

and τ_2. To determine all seven quantities, we invoke also the quadrupole splitting ν_Q^0, given by (4.8) with

$$A_Q = 1 - \tfrac{3}{2}\sigma_2 \ . \tag{6.9}$$

We can now transform the seven experimental data into the seven derived quantities, given in Table IV, along with the propagated experimental errors. We emphasize that we are not fitting model parameters here. Rather, we are making a transformation of the experimental quantities into a set of new quantities more amenable to direct physical interpretation. This transformation relies on the assumed time-scale separation in (4.3), the Lorentzian approximation in (6.1), and the symmetry and topology of the defects, but it is not restricted to a particular defect geometry or a particular dynamic model. In Appendix B we describe how the data transformation is carried out. We also show that it leads to a unique set of derived quantities.

The data transformation has the virtue of separating the spectral density information into nonredundant static (σ_2, σ_4) and dynamic (τ_0, τ_1, τ_2) quantities. Provided that the counterion distribution is uniform over the surface, σ_2 and σ_4 are purely geometric parameters that can be calculated with relative ease even for quite complex microstructures, where a full spectral density calculation would be computationally demanding.

C. Pore geometry

The simplest possible model of pore geometry requires two parameters, specifying the bilayer thickness and the pore diameter. For this class of two-parameter models, the distribution function $\hat{f}(\theta_{CN})$ involves a single dimensionless parameter λ, which determines $\hat{\sigma}_2$ and $\hat{\sigma}_4$. For these uniaxial pore models we take $\lambda = b/a$, with $2b$ the thickness of (the planar portion of) the bilayer and $2a$ the minimum pore diameter (at the midplane of the bilayer), cf. Fig. 6.

For the geometries considered, the quantity σ_2/σ_4 is a monotonic function of λ. Consequently, the experimentally derived quantities σ_2 and σ_4 can be uniquely converted to λ and x, specifying the geometry and density of defects, respectively. We perform this conversion in two steps. First λ is determined from the experimental ratio σ_2/σ_4. With this λ value, $\hat{\sigma}_2$ and $\hat{\sigma}_4$ can be calculated and x determined from the experimental σ_2 or σ_4 by means of (6.8). This procedure is preferred since the propagated experimental uncertainty in σ_2/σ_4 is considerably smaller than that in the individual σ_m (Table IV). Of course, it may happen that no λ value can reproduce the experimental σ_2/σ_4; the model would then be discarded. On the other hand, to be fully consistent with the NMR data, the model must account not only for σ_2 and σ_4, but also for the correlation times τ_n.

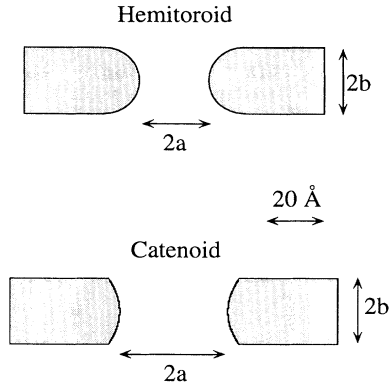

FIG. 6. Cross sections of the hemitoroidal and catenoidal pore geometries with the parameters a and b defined. The shaded regions correspond to the hydrocarbon core of the bilayer, with the dimensions obtained from the analysis in Sec. VI.

We consider two specific pore geometries: the hemitoroidal pore and the catenoidal pore, shown in Fig. 6. In the hemitoroidal pore the defect is healed by a curved lip which forms the inner part of a torus. The geometric parameters are given by

$$\hat{\sigma}_2 = \frac{(\pi/2)(1+\lambda) - \frac{4}{3}\lambda}{\pi(1+\lambda) - 2\lambda} \ , \tag{6.10a}$$

$$\hat{\sigma}_4 = \frac{(3\pi/8)(1+\lambda) - \frac{16}{15}\lambda}{\pi(1+\lambda) - 2\lambda} \ . \tag{6.10b}$$

The other pore model is a truncated catenoid. In contrast to the hemitorus, both principal curvatures c_1 and c_2 are nonuniform on the catenoid. In fact, $c_1 = -c_2$ so that the mean curvature vanishes at every point, just as for a planar bilayer. (The catenoid is the only surface of revolution that is also a minimal surface [66].) Despite the unphysical discontinuity at its boundary, the catenoidal pore model is included here to assess the sensitivity of the NMR data to the detailed curvature distribution within the defect. For the catenoidal pore

$$\hat{\sigma}_2 = \frac{4\lambda}{2\lambda + \sinh(2\lambda)} \ , \tag{6.11a}$$

$$\hat{\sigma}_4 = \frac{4\tanh(\lambda)}{2\lambda + \sinh(2\lambda)} \ . \tag{6.11b}$$

Figure 7 shows the ratio $\sigma_2/\sigma_4 = \hat{\sigma}_2/\hat{\sigma}_4$ versus $\lambda = b/a$, as given by (6.10) and (6.11), for the two pore geometries. Both models are seen to be consistent with the experimental σ_2/σ_4. Since $\hat{\sigma}_2/\hat{\sigma}_4$ varies relatively weakly with λ for the hemitoroidal pore, the propagated uncertainty in λ is large for this model. The deduced values for the two model parameters λ and x, and for several quantities derived therefrom (cf. Sec. VI D), are given in Table V.

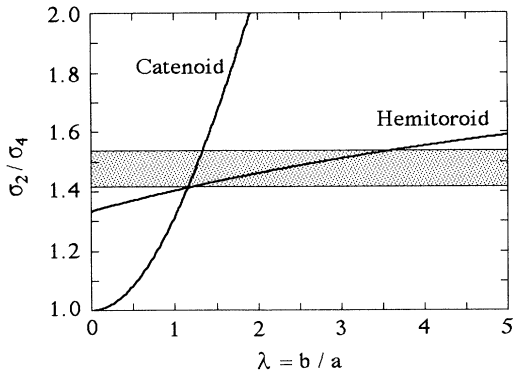

FIG. 7. Ratio of geometric parameters for the hemitoroidal and catenoidal pores in Fig. 6. The shaded band corresponds to the experimental σ_2/σ_4 with propagated random errors (Table IV).

D. Defect density

The oil-continuous bilayer with pores is unique among the three topological types of microstructure: only in this case is the curved area fraction x also a measure of defect density. For bilayers fragmented in one (ribbons) or two (discoids) dimensions, the defect (or aggregate) density can be varied without affecting the curved area fraction x, which is fully determined by the aggregate (ribbon or discoid) shape.

For a bilayer with pores, the curved area fraction x can be converted to more direct measures of defect density. The fraction Γ of the bilayer plane occupied by pores can be obtained from the relation

$$\frac{1/\Gamma-1}{1/x-1}=\frac{\hat{A}}{2\hat{S}}\ , \tag{6.12}$$

with $\hat{A}$ the curved surface area of the pore and $\hat{S}$ the area in the bilayer plane occupied by the defect. For the pore geometries considered here, the right-hand side of (6.12) is a function of λ only. For the hemitoroidal pore,

$$\frac{1/\Gamma-1}{1/x-1}=\frac{\lambda[\pi(1+\lambda)-2\lambda]}{(1+\lambda)^2}\ , \tag{6.13a}$$

and for the catenoidal pore

$$\frac{1/\Gamma-1}{1/x-1}=\frac{2\lambda+\sinh(2\lambda)}{1+\cosh(2\lambda)}\ . \tag{6.13b}$$

A quantity of relevance for the permeability of water and ions through the bilayer is the fraction γ of bilayer plane that is open (when viewed from above). For the hemitoroidal pore,

$$\gamma=\frac{(1+\lambda^2)\Gamma}{\lambda(1+\lambda)}\ , \tag{6.14a}$$

and for the catenoidal pore

$$\gamma=\frac{2\Gamma}{1+\cosh(2\lambda)}\ . \tag{6.14b}$$

Another quantity, of interest in connection with x-ray-diffraction data (cf. Sec. VI E), is the volume fraction Ψ of water in the bilayer, which can be obtained from λ and x through the relation

$$\Psi=\frac{\hat{V}\Gamma}{2b\hat{S}}\ , \tag{6.15}$$

with $\hat{V}$ the aqueous volume contained in a pore. For the hemitoroidal pore,

$$\Psi=\Gamma\left\{1-\frac{\lambda[(\pi/2)(1+\lambda)-\frac{2}{3}\lambda]}{(1+\lambda)^2}\right\}\ , \tag{6.16a}$$

and for the catenoidal pore

$$\Psi=\Gamma\frac{1+\sinh(2\lambda)/(2\lambda)}{1+\cosh(2\lambda)}\ . \tag{6.16b}$$

The four measures of pore density (x, Γ, γ, and Ψ) are given in Table V. The curved area fraction is high, with only $\frac{1}{4}$ (hemitoroidal pores) or $\frac{1}{2}$ (catenoidal pores) of the total surface being planar. It should be remembered that these quantities refer to the hypothetical surface on which the counterions diffuse (cf. Sec. VI E).

TABLE V. Model parameters and derived quantities for uniaxial pores.

Parameter	Derived quantity	Hemitoroidal pore	Catenoidal pore
λ		2.3±1.2	1.26±0.09
x		0.76±0.13	0.48±0.07
	Γ	0.72±0.14	0.43±0.07
	γ	0.06±0.04	0.12±0.02
	Ψ	0.16±0.04	0.21±0.03

E. Pore dimensions

The geometric parameters σ_2 and σ_4 derived from the spin-relaxation data are invariant under isometric scaling of the microstructure, and hence cannot be used to determine its length scales. This can be done, however, by invoking the repeat distance d determined by x-ray diffraction (Sec. II B) or by analyzing the correlation times τ_n. We make the calculation with reference to the dividing surface that separates nonpolar (hydrocarbon chains) and polar (water, counterions, and headgroups) regions. Quantities referring to this partitioning will be given a zero subscript.

The volume fraction ϕ_0 of nonpolar material in the L_α phase can be expressed as

$$\phi_0=(1-\Psi_0)\frac{2b_0}{d}\ . \tag{6.17}$$

From the sample composition and the partial specific volumes (in Å^3) $v(H_2O)=30$, $v(C_{12})=350$, $v(C_{10})=296$, $v(SO_4Na)=57$, and $v(OH)=12$ (the headgroup volumes are obtained by difference from the partial specific volumes of the amphiphiles and that of the hydrocarbon chains [67]), we obtain $\phi_0=0.288$.

To make contact with the spin-relaxation data, which reflect the hypothetical surface on which the strongly confined (Appendix A) counterions diffuse, we assume that this surface has the same analytical shape as the polar/nonpolar dividing surface, but with different di-

mensions according to

$$b-b_0=a_0-a=\delta \ . \tag{6.18}$$

For the hemitoroidal pore the two surfaces are parallel. The displacement parameter δ is taken to be 5 Å. The volume fraction Ψ, referring to the diffusion surface, can be converted to Ψ_0, referring to the dividing surface, by means of the relation

$$\Psi_0=\Psi\frac{b\hat{V}_0}{b_0\hat{V}} \ . \tag{6.19}$$

We thus obtain for the hemitoroidal pore $\Psi_0=0.27\pm0.07$, $a_0=12.2\pm3.8$ Å, and $b_0=11.6\pm1.2$ Å, and for the catenoidal pore $\Psi_0=0.26\pm0.04$, $a_0=17.9\pm1.1$ Å, and $b_0=11.5\pm0.6$ Å. (The drawings in Fig. 6 are based on these dimensions.) Roughly $\frac{1}{4}$ of the bilayer core is thus composed of polar material. As expected, the bilayer half-thickness b_0 is intermediate between the value 8.4 Å, corresponding to a defect-free bilayer [with $\Psi_0=0$ in (6.17)], and the value 16.7 Å, corresponding to a fully extended C_{12} chain [67].

As regards the mean curvature H (cf. Sec. X) and the general shape, the catenoidal pore ($H=0$) is intermediate between the cylindrical pore ($H<0$) and the hemitoroidal pore ($H>0$). While the cylindrical pore can be excluded since it would give $J_{00}^{C,\mathrm{def}}(\omega)=J_{11}^{C,\mathrm{def}}(\omega)\equiv0$ (Sec. IV), only a small deviation from this geometry (cf. the catenoidal pore in Fig. 6) is required to account for the CFSD's. In the following, however, we shall only discuss the hemitoroidal pore, since the other two pore geometries involve unphysical discontinuities.

VII. RIBBONS

A. Spectral densities

We consider now the contributions $J_{nn}^{C,\mathrm{def}}(k\omega_L)$ to the nonadiabatic CFSD's from counterion diffusion over the surface of a ribbon (bounded by two slits) with its axis in the bilayer plane (Fig. 5). We assume that the ribbon axis, i.e., the normal to its cross section, is a twofold axis. The ribbons (but not necessarily the slits) are taken to be monodisperse in size; however, the in-plane orientation of the twofold axis is not required to be uniform. There are two limiting cases: (i) differently oriented two-dimensional domains of straight ribbons of finite length, or (ii) continuously curved ribbons of indefinite length. We assume that the length of the straight ribbons or the radius of curvature (or persistence length) of the curved ribbons is much larger than the bilayer thickness. Counterion diffusion along the length of the ribbon may then contribute to the adiabatic CFSD's, whereas only counterion diffusion around the ribbon contributes to the nonadiabatic CFSD's.

If the counterions did not diffuse from one ribbon to another, the surface-diffusion contributions to the nonadiabatic CFSD's would be different for ribbons with different in-plane orientation. However, if this orientational distribution is sampled on a time scale that is short compared to the corresponding variation in spin-relaxation rates, then one observes the orientationally averaged CFSD's. To be consistent with the assumed uniaxial relaxation behavior (Sec. III), the sampled orientational distribution of ribbon axes must exhibit at least fivefold symmetry [46].

Since the ribbons are locally straight, the surface normal is everywhere perpendicular to the twofold axis. Surface diffusion around the ribbon is then described by the two ribbon-frame spectral density (RFSD) functions [46]

$$J_A^R(k\omega_L)=\tfrac{3}{4}\pi^2\bar{\chi}^2\int_0^\infty dt\cos(k\omega_L t)\times[\langle\cos(2\phi_R^0)\cos(2\phi_R)\rangle-\langle\cos(2\phi_R)\rangle^2] \ , \tag{7.1a}$$

$$J_B^R(k\omega_L)=\tfrac{3}{4}\pi^2\bar{\chi}^2\int_0^\infty dt\cos(k\omega_L t)\times\langle\sin(2\phi_R^0)\sin(2\phi_R)\rangle \ , \tag{7.1b}$$

with ϕ_R the angle around the ribbon axis. The symmetry indices A and B refer to the irreducible representations A_1 and B_1 of the symmetry group D_{2h} of the ribbon [46].

The six nonadiabatic CFSD's can be expressed in terms of J_{loc} and the four RFSD's as [46]

$$J_{00}^C(k\omega_L)=J_{\mathrm{loc}}+\tfrac{3}{4}J_A^R(k\omega_L) \ , \tag{7.2a}$$

$$J_{11}^C(k\omega_L)=J_{\mathrm{loc}}+\tfrac{1}{2}J_B^R(k\omega_L) \ , \tag{7.2b}$$

$$J_{22}^C(k\omega_L)=J_{\mathrm{loc}}+\tfrac{1}{8}J_A^R(k\omega_L) \ . \tag{7.2c}$$

At each frequency ($k=1$ or 2), we can thus solve for J_{loc}, $J_A^R(k\omega_L)$, and $J_B^R(k\omega_L)$. The results, given in Table VI, show that the data are consistent with the general assumptions made so far (since J_{loc} is independent of k), and that the ribbon cross section is distinctly noncircular [since $J_A^R(k\omega_L)\neq J_B^R(k\omega_L)$].

To separate static and dynamic information, we now invoke the Lorentzian approximation

$$J_S^R(k\omega_L)=\pi^2\bar{\chi}^2A_S\frac{\tau_S}{1+(k\omega_L\tau_S)^2} \ , \tag{7.3}$$

with $S=A$ or B. The amplitude factors are

$$A_A=3(\sigma_4-\sigma_2^2) \ , \tag{7.4a}$$

$$A_B=3(\sigma_2-\sigma_4) \ , \tag{7.4b}$$

with

$$\sigma_m=\langle\sin^m\phi_R\rangle=\int_0^{2\pi}d\phi_R f(\phi_R)\sin^m\phi_R \ , \tag{7.5}$$

with $\phi_R=0$ on the planar part of the ribbon. In the limit of a circular cross section, $A_A=A_B=\frac{3}{8}$ and (7.3) is exact [41–43].

TABLE VI. Ribbon-frame spectral densities derived from the nonadiabatic CFSD's assuming ribbons with twofold symmetry.

k	J_{loc} (s^{-1})	$J_A^R(k\omega_L)$ (s^{-1})	$J_B^R(k\omega_L)$ (s^{-1})
1	21.4±3.4	71.4±7.6	49.6±7.2
2	21.6±0.6	51.4±3.7	36.0±2.8

B. Data transformation

Having already determined J_{loc}, there remains five quantities ($\bar{\chi}$, σ_2, σ_4, τ_A, and τ_B) to be determined from the four RFSD's in Table VI and the quadrupole splitting. The correlation times τ_A and τ_B are obtained directly from (7.3), without invoking the splitting. As seen from Table VII, $\tau_A=\tau_B$ within the experimental uncertainty.

The quadrupole splitting is still given by (4.8) and (6.9), i.e.,

$$\nu_Q^0=\tfrac{1}{2}(1-\tfrac{3}{2}\sigma_2)\bar{\chi} \ . \tag{7.6}$$

To obtain this result, we have also averaged over the in-plane orientation of the ribbon axis. (This orientation must be distributed with at least threefold symmetry, since the line shape obtained from a powder sample is of the uniaxial type.)

In contrast to the case of uniaxial pores (Appendix B), the data transformation does not produce a unique set $(\bar{\chi},\sigma_2,\sigma_4)$ in the case of the ribbon microstructure. Since we can only determine the magnitude $|\nu_Q^0|$ of the quadrupole splitting, two different sets of parameter values may be consistent with the data. As seen from Table VII, however, the set corresponding to $\nu_Q^0<0$ can be discarded on physical grounds: the large σ_2 and σ_4 imply that nearly all surfaces are perpendicular to the L_α phase director. (The much larger residual QCC $\bar{\chi}$, as compared to the nearby H_α phase [42,43], also speaks against this alternative.) A comparison with Table IV shows that the derived quantities do not differ significantly from those derived assuming a bilayer with uniaxial pores. However, the geometric interpretation of the parameters σ_2 and σ_4 is of course different for the two microstructures.

C. Elliptic ribbon

To obtain a geometric interpretation of the quantities σ_2 and σ_4 for the ribbon microstructure, we assume that the cross section is a rectangle with semiellipses on two sides. This elliptic ribbon model involves three length scales: a, b, and c, defined in Fig. 8. The cross-sectional shape, and hence σ_2 and σ_4, is determined by two dimensionless parameters, which we choose as $\eta=c/b$, the aspect ratio of the rectangular part, and $\rho=a/b$, the axial ratio of the elliptic part. The elliptic ribbon reduces to an elliptic cylinder for $\eta=0$, and to a circular cylinder for $\eta=0$ and $\rho=1$.

As in the case of pores, we can write

TABLE VII. Quantities derived from the quadrupole splitting and the RFSD's assuming ribbons with twofold symmetry.

Quantity	$\nu_Q^0>0$	$\nu_Q^0<0$
τ_A (ns)	2.3±0.7	2.3±0.7
τ_B (ns)	2.3±0.8	2.3±0.8
σ_2	0.25±0.02	0.92±0.01
σ_4	0.17±0.01	0.89±0.01
σ_2/σ_4	1.45±0.06	1.03±0.01
$\lvert\bar{\chi}\rvert$ (kHz)	104±4	168±4

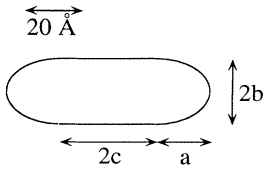

FIG. 8. Cross section of the elliptic ribbon geometry with the parameters a, b, and c defined. The shaded region corresponds to the hydrocarbon core of the ribbon, with the dimensions obtained from the analysis in Sec. VII and a displacement parameter $\delta=5$ Å.

$$\sigma_m=x\hat{\sigma}_m \ , \tag{7.7}$$

where x is the fraction curved surface on the ribbon and $\hat{\sigma}_m$ refers to the curved (elliptic) part of the ribbon. Whereas σ_m depends on η and ρ, $\hat{\sigma}_m$ depends only on ρ. We can thus determine ρ from the ratio σ_2/σ_4 and then obtain η from (7.7). The defect density, however, cannot be determined as this requires knowledge of the slit width (Sec. VI E).

For the elliptic ribbon, we obtain

$$x=\left[1+\frac{\eta}{\rho E}\right]^{-1} , \tag{7.8a}$$

$$\hat{\sigma}_2=(K/E-1)/(\rho^2-1) \ , \tag{7.8b}$$

$$\hat{\sigma}_4=(1+\rho^2-2K/E)/(\rho^2-1)^2 \ , \tag{7.8c}$$

where K and E are the complete elliptic integrals of the first and second kind with modulus $\sqrt{1-\rho^{-2}}$. Figure 9 shows the ratio $\sigma_2/\sigma_4=\hat{\sigma}_2/\hat{\sigma}_4$ versus the axial ratio ρ of the ellipse: σ_2/σ_4 increases monotonically with ρ from the value $\frac{4}{3}$ at $\rho=1$ (circular cylinder). The data are seen to be consistent with an elliptic ribbon geometry with $\rho=1.4\pm0.2$ and $\eta=1.0\pm0.3$. (It may be noted that the $\nu_Q^0<0$ solution, with $\sigma_2/\sigma_4<\frac{4}{3}$, is inconsistent with an elliptic ribbon geometry.)

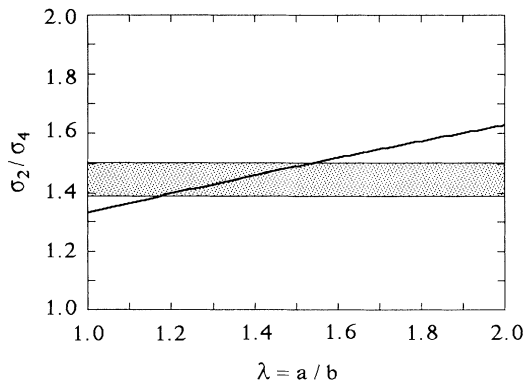

FIG. 9. Ratio of geometric parameters for the elliptic ribbon in Fig. 8. The shaded band corresponds to the experimental σ_2/σ_4 with propagated random errors (Table VII).

VIII. DISCOIDS

A. Spectral densities

We consider now the contributions $J_{nn}^{C,\mathrm{def}}(k\omega_L)$ to the nonadiabatic CFSD's from counterion diffusion over the surface of orientationally disordered micelles. Restricted micelle reorientation does not contribute significantly to the nonadiabatic CFSD's since it is much slower than the surface diffusion, but acts only to average the orientation-dependent micelle-frame surface-diffusion spectral densities over the orientational distribution for the angle θ_{CM} between the micelle symmetry axis and the L_α phase director [44,45]. In this limit the smectic translational order (layering) of the micelles does not directly affect the nonadiabatic CFSD's.

An efficient numerical scheme for calculating the spectral densities $J_{nn}^{M}(k\omega_L)$ in the case of oblate and prolate spheroidal micelles has recently been developed [54], and applied to ^{2}H and ^{23}Na spin-relaxation data from the two nematic phases in the present lyotropic system [44]. Since we do not want to restrict the analysis to this particular micelle geometry, however, we invoke the Lorentzian approximation for $J_{nn}^{C,\mathrm{def}}(k\omega_L)$, i.e., we express the nonadiabatic CFSD's in the form

$$J_{nn}^{C}(k\omega_L)=J_{\mathrm{loc}}+\pi^2\bar{\chi}^2\alpha_n\frac{\tau_n}{1+(k\omega_L\tau_n)^2}\ . \tag{8.1}$$

The amplitude factors α_n in (8.1) can be expressed as

$$\alpha_0=\tfrac{1}{5}[\,(1+\tfrac{10}{7}S+\tfrac{18}{7}Q)A_0+(2+\tfrac{10}{7}S-\tfrac{24}{7}Q)A_1 +(2-\tfrac{20}{7}S+\tfrac{6}{7}Q)A_2\,]\ , \tag{8.2a}$$

$$\alpha_1=\tfrac{1}{5}[\,(1+\tfrac{5}{7}S-\tfrac{12}{7}Q)A_0+(2+\tfrac{5}{7}S+\tfrac{16}{7}Q)A_1 +(2-\tfrac{10}{7}S-\tfrac{4}{7}Q)A_2\,]\ , \tag{8.2b}$$

$$\alpha_2=\tfrac{1}{5}[\,(1-\tfrac{10}{7}S+\tfrac{3}{7}Q)A_0+(2-\tfrac{10}{7}S-\tfrac{4}{7}Q)A_1 +(2+\tfrac{20}{7}S+\tfrac{1}{7}Q)A_2\,]\ , \tag{8.2c}$$

with the micelle order parameters

$$S=\langle P_2(\cos\theta_{CM})\rangle\ , \tag{8.3a}$$

$$Q=\langle P_4(\cos\theta_{CM})\rangle\ , \tag{8.3b}$$

and the micelle-frame amplitude factors A_n, related via (6.4) to the geometric parameters $\sigma_m=\langle\sin^m\theta_{MN}\rangle$, with θ_{MN} the angle between the local surface normal and the micelle symmetry axis.

By means of (6.4) and (8.2), the three independent amplitude factors α_n can thus be expressed in terms of the four independent parameters σ_2, σ_4, S, and Q. In the limit of complete orientational order ($S=Q=1$), the α_n reduce to the corresponding A_n.

B. Data analysis

In the limit of complete orientational order ($S=Q=1$), the geometry-independent part of the analysis in Sec. VI, and the results in Table IV, are valid also for the discoidal microstructure. In general, however, we now have nine unknown quantities (J_{loc}, $\bar{\chi}$, τ_0, τ_1, τ_2, σ_2, σ_4, S, and Q), which obviously cannot be determined from the six CFSD's and the quadrupole splitting, now given by

$$\nu_Q^0=\tfrac{1}{2}S(1-\tfrac{3}{2}\sigma_2)\bar{\chi}\ . \tag{8.4}$$

To proceed we introduce two constraints that provide unique relationships between S and Q and between σ_2 and σ_4. These constraints are introduced in the form of one-parameter orientational distribution functions for the angles θ_{CM} and θ_{MN}, respectively. The former is taken to be of the form

$$f(\theta_{CM})\sim\exp(-u\sin^2\theta_{CM})\ , \tag{8.5}$$

which, for the high degrees of order of interest here, amounts to retaining the leading term in an expansion of the potential of mean torque in powers of θ_{CM}. (The linear term vanishes by symmetry.) This should be a highly accurate approximation here [44].

For a given micelle order parameter S [which also fixes Q through (8.5)], we can now calculate the seven quantities J_{loc}, $\bar{\chi}$, τ_0, τ_1, τ_2, σ_2, and σ_4 using (6.4), (8.1), (8.2), and (8.4) in an iterative scheme similar to that described in Appendix B. The ratio σ_2/σ_4 obtained in this way is shown in Fig. 10 as a function of the order parameter S. Note that in the limit $S=1$, the discoid case becomes formally identical to the uniaxial pore, with the parameters given in Table IV.

To uniquely determine S, and hence the other eight quantities, we invoke the second constraint, which amounts to a specification of the geometry of the discoidal micelle. We consider two geometries: an oblate spheroid and a hemitoroidal disk. (In the latter the aggregate comprises a central cylindrical disk with a hemitoroidal edge.) For these geometries, σ_2 and σ_4 are both determined by the axial ratio ρ. For a hemitoroidal disk of thickness $2b$ and diameter $2R+2b$,

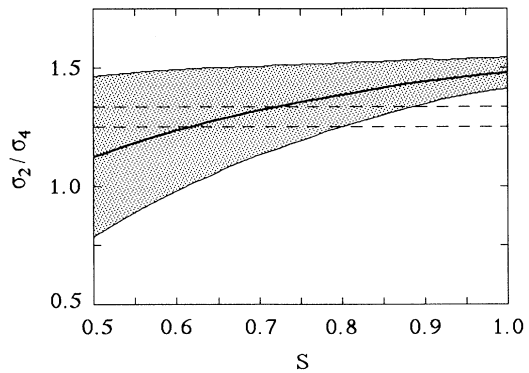

FIG. 10. Experimentally derived ratio of geometric parameters for discoidal micelles vs the micelle order parameter S. The shaded area represents the propagated random errors. The dashed lines are theoretical bounds on σ_2/σ_4 for specific geometries (cf. text).

$$\sigma_2=\frac{(\pi/2)\xi+\frac{4}{3}}{\xi(\xi+\pi)+2}\ , \tag{8.6a}$$

$$\sigma_4=\frac{(3\pi/8)\xi+\frac{16}{15}}{\xi(\xi+\pi)+2}\ , \tag{8.6b}$$

with $\xi\equiv\rho-1=R/b$. For an oblate spheroid of major and minor semiaxes a and b [54],

$$\sigma_2=\frac{(2\rho^2-1)\mu-2\rho^2}{(\rho^2-1)\mu}\ , \tag{8.7a}$$

$$\sigma_4=\frac{(1-4\rho^2)\mu+6\rho^2}{(\rho^2-1)^2\mu}\ , \tag{8.7b}$$

with $\rho=a/b$ and

$$\mu=1+\frac{\operatorname{arccosh}(\rho)}{\rho\sqrt{\rho^2-1}}\ . \tag{8.7c}$$

For both geometries, the lower bound on σ_2/σ_4 is $\frac{5}{4}$, corresponding to the sphere limit. For the hemitoroidal disk there is also a finite upper bound, restricting σ_2/σ_4 to the narrow range

$$\tfrac{5}{4}\le\sigma_2/\sigma_4\le\tfrac{4}{3}\ . \tag{8.8}$$

Since σ_2 and σ_4 are both determined by ρ, we can now attempt to find a solution, i.e., a set of values for the seven parameters $J_{\rm loc}$, $\bar{\chi}$, τ_0, τ_1, τ_2, S, and ρ, that reproduces the six CFSD's and the splitting. Such a solution exists for the hemitoroidal disk, but not for the oblate spheroid. For the hemitoroidal disk the results are given in Table VIII. For the oblate geometry, the closest agreement is obtained with $S=1$, where $\sigma_2/\sigma_4=1.48\pm0.06$ (cf. Table IV and Fig. 10) corresponding to an axial ratio $\rho=1.9$. With $\rho=1.9$, however, (8.7) yields values for the individual σ_2 and σ_4 that are 50% larger than the experimentally derived results in Table IV.

C. Complete spectral density calculation

The accuracy of the Lorentzian approximation (8.1) can be checked by exactly calculating the spectral density functions $J_{nn}^{C,\rm def}(\omega)$ for surface diffusion on orientationally disordered oblate spheroids [54]. Two examples of exact dispersion curves are shown in Fig. 11. For $\rho=2$ the Lorentzian approximation is highly accurate, whereas for $\rho=6$ there is a pronounced deviation from a Lorentzian dispersion at the frequencies ω_L and $2\omega_L$ probed by the nonadiabatic CFSD's. (Similar results are obtained for the spectral densities with symmetry index $n=1$ and 2, and for order parameters $S<1$.)

TABLE VIII. Quantities derived from the quadrupole splitting and the nonadiabatic CFSD's assuming hemitoroidal disks.

Quantity	Value
$J_{\rm loc}$ (s^{-1})	13±9
$\lvert\bar{\chi}\rvert$ (kHz)	136±40
σ_2	0.21±0.05
σ_4	0.16±0.04
σ_2/σ_4	1.32±0.01
τ_0 (ns)	2.1±0.5
τ_1 (ns)	1.8±0.6
τ_2 (ns)	1.4±0.4
S	0.70±0.26
ρ	6.0±1.6

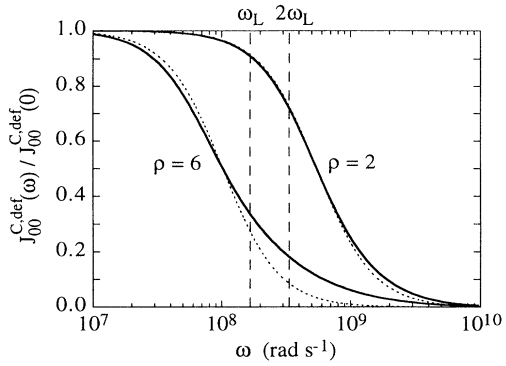

FIG. 11. Frequency dispersion of the spectral density function $J_{00}^{C,\rm def}(\omega)$ for surface diffusion on oblate spheroids of the indicated axial ratio ρ, $S=1$, and $\tau_s=b^2/D_s=5$ ns. The dashed curves are Lorentzian dispersions, with the correlation time τ_0 chosen so that $J_{00}^{C,\rm def}(1/\tau_0)=J_{00}^{C,\rm def}(0)/2$. The vertical lines indicate the frequencies probed by the nonadiabatic CFSD's.

The failure of the oblate spheroid model in accounting for the individual σ_2 and σ_4 values (Sec. VIII B) is thus not due to a breakdown of the Lorentzian approximation (8.1). This failure can be exhibited even more conclusively, without invoking the Lorentzian approximation, by calculating the quantities

$$\Lambda_k\equiv\frac{J_{00}^{C}(k\omega_L)-J_{\rm rad}^{C}-J_{11}^{C}(k\omega_L)}{J_{11}^{C}(k\omega_L)-J_{22}^{C}(k\omega_L)}=\frac{J_{00}^{C,\rm def}(k\omega_L)-J_{11}^{C,\rm def}(k\omega_L)}{J_{11}^{C,\rm def}(k\omega_L)-J_{22}^{C,\rm def}(k\omega_L)}\ , \tag{8.9}$$

which are independent of $J_{\rm loc}$ and $\bar{\chi}$ and depends only on the micelle order parameter S, the axial ratio ρ, and the diffusional time constant $\tau_s=b^2/D_s$.

Figure 12 shows Λ_1 and Λ_2 as functions of ρ for $\tau_s=5$ ns and $S=0.7$ or 1.0. As the spherical ($\rho=1$) limit is ap-

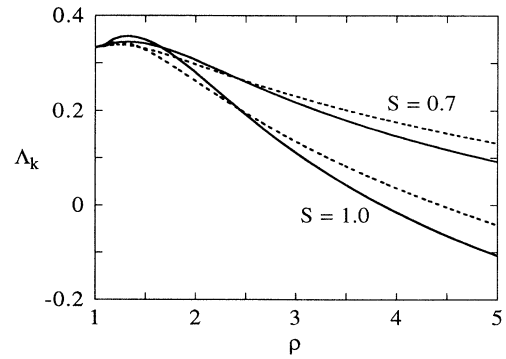

FIG. 12. Calculated spectral density difference ratios Λ_1 (solid) and Λ_2 (dashed), defined by (8.9), for surface diffusion on orientationally disordered oblate spheroids of axial ratio ρ and orientational order parameter S. The diffusion time constant is $\tau_s=b^2/D_s=5$ ns.

proached, Λ_k becomes less dependent on τ_s and S, with the limiting value $\Lambda_k = \frac{1}{3}$ being entirely independent of τ_s and S. For any reasonable choice of τ_s (1–10 ns) and S (0.5–1.0), Λ_k therefore does not exceed 0.4. From the CFSD's in Table III we obtain $\Lambda_1 = \Lambda_2 = 1.8 \pm 0.4$ for $J_{\text{rad}} = 0$ and $\Lambda_1 = 1.2 \pm 0.4$, $\Lambda_2 = 0.9 \pm 0.3$ for a maximal radial contribution (Appendix A) of $J_{\text{rad}} = 10\ \text{s}^{-1}$. It is therefore clear that the oblate spheroidal microstructure can be excluded. (A similar analysis also rules out a microstructure of prolate spheroidal aggregate with the symmetry axis isotropically distributed within the smectic plane.)

For the hemitoroidal disk, we did arrive at an internally consistent solution in Sec. VIII B. It is clear from Fig. 11, however, that the Lorentzian approximation (8.1) breaks down for an axial ratio as large as $\rho = 6$. (This conclusion should hold for disks as well as for oblates.) Therefore, we must reject the results in Table VIII as artifacts of the Lorentzian approximation. Instead we argue that the Λ_k curves in Fig. 12 should *not* depend strongly on whether the micelle is an oblate spheroid or a hemitoroidal disk. In particular, the $\rho = 1$ limit of $\Lambda_k = \frac{1}{3}$ must be the same and the decrease in Λ_k for large ρ should remain. In view of the large experimental Λ_k values (cf. above), we therefore conclude that *the relaxation data rule out a microstructure of water-continuous bilayers with discoidal micelles.*

IX. DEFECT ENERGETICS

In the preceding analysis of spin-relaxation data, we considered three topological types of bilayer defect: pores, ribbons, and discoids. Defect geometries of the first two types were found to be consistent with the relaxation data *for certain values of the relative defect dimensions.* We shall now attempt to discriminate among these structural alternatives on the basis of their relative stability. To this end we adopt a phenomenological approach where the dominant contribution to the free energy of defect formation is identified with the curvature energy of the amphiphilic monolayers. Despite its simplicity, this approach usually provides at least a qualitative understanding of the relation between interface geometry and energetics in lyotropic systems [68–71]. Other energy contributions are briefly discussed in Sec. IX B.

A. Curvature energy

If the relevant interactions are of sufficiently short range, the curvature energy can be expressed as the integral, over the monolayer surface, of a curvature energy density g_c (per unit area of monolayer) of the form [68,72,73]

$$g_c(x_1,x_2) = \tfrac{1}{2}\kappa(x_1+x_2)^2 + \bar{\kappa}x_1x_2 \ . \tag{9.1}$$

These are the leading terms in an expansion in the curvature *deviations* $x_i = c_i - c_{\text{eq}}$, with c_1 and c_2 the principal curvatures and c_{eq} the equilibrium curvature. In the absence of other constraints, the monolayer would thus prefer a *locally* spherical geometry with $c_1 = c_2 = c_{\text{eq}}$. (For simplicity and on physical grounds, we disregard the possibility of having two unequal equilibrium curvatures [73].) For the monolayer geometries to be considered, the curvature deviations x_i are not uniformly small compared to the inverse monolayer thickness. The neglect of higher-order terms [74] is justified by simplicity and the hope that these contributions tend to cancel on average. (Certain higher-order contributions involve the curvature gradient [75], which diverges at points where flat and curved surfaces are joined.)

The curvature-elastic moduli (with dimension of energy) in (9.1) are the splay elasticity (or bending rigidity) κ and the saddle-splay elasticity $\bar{\kappa}$. These moduli are subject to certain restrictions, which can be directly displayed by expressing (9.1) as a canonical quadratic form

$$g_c(x_1,x_2) = \tfrac{1}{4}(2\kappa+\bar{\kappa})(x_1+x_2)^2 - \tfrac{1}{4}\bar{\kappa}(x_1-x_2)^2 \ . \tag{9.2}$$

In order for the equilibrium state $x_1 = x_2 = 0$ to be stable, the quadratic form (9.2) must be positive definite and, hence, must have positive eigenvalues, implying that

$$\kappa > 0 \ , \tag{9.3a}$$

$$-2\kappa < \bar{\kappa} < 0 \ . \tag{9.3b}$$

It is convenient to change the independent variables c_1 and c_2 to the mean and Gaussian curvatures $H = (c_1+c_2)/2$ and $K = c_1c_2$. Omitting a physically irrelevant constant term, we then obtain from (9.1)

$$g_c(H,K) = 2\kappa H^2 - 2(2\kappa+\bar{\kappa})c_{\text{eq}}H + \bar{\kappa}K \ . \tag{9.4}$$

This expression contains three phenomenological parameters: κ, $\bar{\kappa}$, and c_{eq}. They are usually obtained experimentally, but can in principle be calculated from the relevant microscopic interactions [69,76,77]. This choice of parameters, however, is not unique. In fact, in the traditional approach, due to Helfrich [68,72], the third parameter is chosen as the spontaneous curvature c_0, related to the equilibrium curvature c_{eq} through

$$c_0 = \left[2 + \frac{\bar{\kappa}}{\kappa}\right] c_{\text{eq}} \ . \tag{9.5}$$

We prefer to work with c_{eq}, which has a direct geometrical significance, rather than with the thermodynamic quantity c_0 [70,73].

The Gaussian curvature term in the curvature energy density (9.4) is usually omitted since, when integrated over a closed simply connected surface, it reduces to a constant that depends only on the topology of the surface. This is a consequence of the Gauss-Bonnet theorem [66], which implies that

$$\int dA\ K = 2\pi\chi_E = 4\pi(1-g) \ , \tag{9.6}$$

with χ_E the Euler-Poincaré characteristic of the surface and g its genus [66]. Since the structural defects considered here alter the topology of the monolayer, the Gaussian curvature term can play an important role. Consider the contribution (9.6) to the curvature energy obtained by integrating (9.4) over the total interfacial

area A of a defective bilayer of indefinite lateral extent. Discoids and ribbons (with closed ends) are topologically equivalent to spheres ($g=0$), whence (9.6) yields $4\pi N$ for a bilayer containing N discoids or ribbons. A bilayer (with closed edges) containing N pores has $g=N$, whence (9.6) yields $-4\pi N$ for $N \gg 1$.

Averaging (9.4) over a large patch of bilayer and using (9.6), we obtain

$$\langle g_c \rangle = \frac{1}{A}\int dA\, g_c(H,K) = 2\kappa\langle H^2\rangle - 2(2\kappa+\bar{\kappa})c_{\rm eq}\langle H\rangle \pm 4\pi\bar{\kappa}\frac{N}{A}\ , \qquad (9.7)$$

with the minus sign pertaining to pores. If the ribbons are sufficiently long, the area per defect A/N becomes so large that the last term in (9.7) can be neglected. (This is in keeping with the neglect of ribbon end effects in Sec. VII.) The reference for the curvature energy density in (9.4) and (9.7) is the classical bilayer, for which $\langle g_c \rangle = 0$.

Using the relative dimensions of hemitoroidal pores and elliptic ribbons, as obtained from the spin-relaxation data (Secs. VI and VII), we can now calculate A/N, $\langle H \rangle$, and $\langle H^2 \rangle$, reduced by the appropriate power of the monolayer thickness b to make all quantities dimensionless. Note that $\langle H \rangle$ and $\langle H^2 \rangle$ are averaged over the curved as well as the planar parts of the monolayer surface. Since the relative dimensions obtained in Secs. VI and VII refer to the Na^+ diffusion surface, we convert them to the hydrocarbon-water interface using a displacement parameter $\delta = 5$ Å (Sec. VI E). This interface should be a better approximation to the neutral surface, where the curvatures should properly be evaluated [68,70,75,77]. (The neutral surface is the surface, within the monolayer, whose area is invariant under bending.) In order to compare the curvature energy of different microstructures, we assume that the monolayer thickness b is the same in all cases (cf. Sec. IX B).

As seen from Table IX, the average mean curvature $\langle H \rangle$ is positive for both defect geometries, as in the nearby N_D, N_C, and H_α phases. (Since a pore has principal curvatures of opposite sign, $\langle H \rangle$ may be negative if the pore diameter is sufficiently small compared to the bilayer thickness. For the hemitoroidal pore, $\langle H \rangle < 0$ for $b/a > 6.45$.)

According to (9.7), the *relative* stability of the three interface geometries considered (pores, ribbons, and a classical bilayer) is determined by two dimensionless parameters, which we choose as the reduced equilibrium curvature $c_{\rm eq}b_0$ and the elasticity ratio $\bar{\kappa}/(2\kappa)$. We thus construct the stability diagram in Fig. 13. As seen from (9.3), the elasticity ratio is confined to the range $[-1,0]$. The equilibrium curvature may be estimated from the known interface geometry in the neighboring discotic nematic (N_D) phase (Fig. 1). We have previously concluded, from a combined ^2H and ^{23}Na spin-relaxation study [45], that the N_D phase (at a composition not too far from the present L_α sample) is composed of discoidal micelles (modeled as oblate spheroids) of axial ratio 3–4, corresponding to an average mean curvature $\langle H \rangle b_0$ of 0.3–0.4. Assuming that $\langle H \rangle \approx c_{\rm eq}$ in the N_D phase and noting that $c_{\rm eq}$ must decrease on addition of decanol (going from N_D to L_α), we may regard this value as an approximate upper bound on $c_{\rm eq}b_0$ in our L_α sample. The conclusion from Fig. 13 is then that the ribbon geometry can be stable relative to the classical bilayer if $\bar{\kappa} \geq -1.3\kappa$, while the pore geometry has a higher curvature energy over the full $\bar{\kappa}/(2\kappa)$ range. (The hemitoroidal disk with $\rho = 6$ would require $c_{\rm eq}b_0 > 1.7$ to be stable.) A sufficient condition for the classical bilayer to be stable is that either $c_{\rm eq} = 0$ or $\bar{\kappa} = -2\kappa$. This follows directly from (9.2) and (9.3). (In the case $\bar{\kappa} = -2\kappa$, any monolayer geometry with $c_1 \neq c_2$ at some point has a higher curvature energy than the classical bilayer.)

The stability diagram in Fig. 13 tells us which of the considered geometries is the most stable one, but does not say *how* stable it is. To say this we need to specify the individual elasticities κ and $\bar{\kappa}$. For the L_α phase of the present lyotropic system, the *bilayer* bending rigidity κ_b has recently been determined [78] to be $\kappa_b = 13 \pm 2\ k_B T$ in a sample of considerably higher decanol content ($n_{\rm dec}/n_{\rm SDS} = 2.55$) than in our L_α sample ($n_{\rm dec}/n_{\rm SDS} = 0.467$). Since the bending rigidity is expected to increase on reducing the decanol content, a reasonable estimate for our L_α sample is $\kappa_b \approx 20\ k_B T$. (At the higher decanol content, the bilayer is probably classical [79]. Whereas defects should reduce the *macroscopic* splay modulus, we regard κ as a microscopic quantity.)

TABLE IX. Geometric quantities, related to the curvature energy, for hemitoroidal pores and elliptic ribbons with relative dimensions as determined from the spin-relaxation data.

Quantity	Pore[a]	Ribbon[b]
$\langle H \rangle b_0$	0.35	0.14
$\langle H^2 \rangle b_0^2$	0.23	0.04
$\pm 4\pi N b_0^2/A$	−0.33	0

[a] $\lambda_0 = 0.95$.
[b] $\eta_0 = 1.4$ and $\rho_0 = 1.6$.

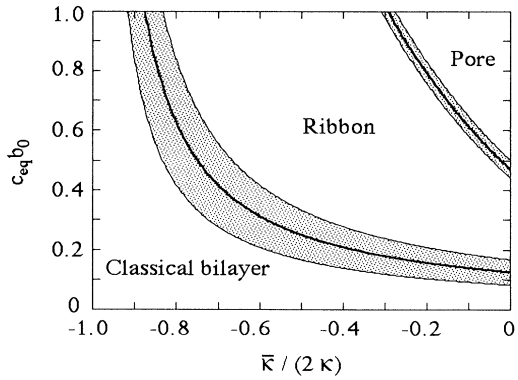

FIG. 13. Stability diagram showing the microstructure of lowest curvature energy for given values of the reduced equilibrium curvature $c_{\rm eq}b_0$ and the elasticity ratio $\bar{\kappa}/(2\kappa)$. The relative dimensions of the ribbon and pore geometries are those determined from the spin-relaxation data (displayed in Figs. 6 and 8). The shaded bands correspond to a stability margin of $\pm 0.1\ k_B T$ per amphiphile, assuming $\kappa = 10\ k_B T$.

To estimate the curvature energy g_c^A per amphiphile, we multiply $\langle g_c \rangle$ in (9.7) by an average area $\bar{s}_A$ per amphiphile at the hydrocarbon-water interface. Taking $\bar{s}_A = 50$ Å^2 and $\kappa = \kappa_b/2 = 10\ k_BT$, we calculate the regions in the $c_{eq}b_0 - \bar{\kappa}/(2\kappa)$ plane where the curvature energy of two geometries differs by less than $0.1k_BT$ per amphiphile. These are shown in Fig. 13 as shaded bands. As long as $c_{eq} > 0$, the ribbon geometry is never more than $0.3k_BT$ above the classical bilayer. In contrast, the pore geometry is $\sim 2k_BT$ above the classical bilayer for $c_{eq} = 0$ or $\bar{\kappa} = -2\kappa$. For $c_{eq}b_0 = 0.3$ and $\bar{\kappa}/(2\kappa) = -0.2$, the curvature energy of classical bilayer and pore is 0.3 and $1.3k_BT$ (per amphiphile), above the ribbon.

B. Other contributions to defect energy

The curvature energy is not the only contribution to the free energy of defect formation. In particular, one should consider the role of interbilayer repulsion, which is responsible for the stability of the L_α phase. As recently emphasized by Bagdassarian *et al.* [80], this repulsion tends to stabilize the classical bilayer against defects since incorporation of water in the bilayer reduces the interbilayer separation, thus enhancing the repulsion.

In our L_α sample, the interbilayer repulsion is essentially of electrostatic origin. The electrostatic contribution, g_{es}, to the free-energy density (per unit area of monolayer), is readily obtained from the Poisson-Boltzmann potential (A6). Under the assumptions specified in Appendix A, one obtains [81]

$$g_{es}(b_w) = \frac{k_BT}{2\pi\lambda_B} \int_{b_w}^{\infty} db_w \lambda_D^{-2} , \tag{9.8}$$

with $2b_w$ the thickness of the aqueous lamella, λ_B the Bjerrum length (7.14 Å at 25 °C), and λ_D the Debye length, obtained from (A7). In the strong-coupling limit, where the Gouy-Chapman length λ_{GC} is much smaller than b_w, we can set $\lambda_D = 2b_w/\pi$ and (9.8) yields

$$g_{es}(b_w) = \frac{\pi k_BT}{8\lambda_B b_w} . \tag{9.9}$$

This strong-coupling approximation overestimates g_{es} by a relative amount of order λ_{GC}/b_w. Since $\lambda_{GC} \approx 1$ Å in our case (and since we only consider energy differences), the error is negligible.

As regards the electrostatic interbilayer repulsion, the introduction of defects has two consequences. First, adjacent bilayers are brought closer together, i.e., b_w is reduced. Second, the effective surface charge density becomes nonuniform. The second effect is probably negligible since g_{es} is independent of the charge density in the strong-coupling limit.

The interbilayer separation $2b_w$ is obtained from

$$d = 2b_0 + 2b_w , \tag{9.10}$$

with $d = 58.6$ Å the lamellar repeat distance (Sec. II B) and $2b_0$ the bilayer core thickness. For the hemitoroidal pore, we obtained $b_0 = 11.6$ Å (Sec. VI E) and we use this value also for the ribbon. The contribution to the free energy of defect formation is

$$\Delta g_{es} = g_{es}(b_w) - g_{es}(b_w^{cl}) , \tag{9.11}$$

where b_w^{cl} refers to a classical bilayer. Assuming that b_0 is the same in the absence of defects (cf. below), we can obtain b_w^{cl} from (9.10) with d replaced by

$$d_{cl} = \frac{d}{1 - \Psi_0} , \tag{9.12}$$

with Ψ_0 the volume fraction water, counterions, and headgroups within the bilayer core. For the pore geometry, we obtained $\Psi_0 = 0.27$ in Sec. VI E; this value also applies to the other geometries since b_0 is taken to be the same [cf. (6.17)].

Using (9.9)–(9.12), we obtain $\Delta g_{es} = 0.06k_BT$ per amphiphile (with $\bar{s}_A = 50$ Å^2 as in Sec. IX A). Despite the 40% reduction of the interbilayer separation, interbilayer repulsion thus plays a minor role as compared to the curvature energy. Referring to the stability diagram in Fig. 13, inclusion of g_{es} would shift the boundary between the classical bilayer and ribbon domains by about $\frac{1}{3}$ of the width of the shaded band. (As long as b_0 is the same, the relative stability of the pore, ribbon, and disk geometries is not affected at all.) However, as we move to lower water contents in the L_α phase, interbilayer repulsion (electrostatic and hydration) will eventually dominate the free energy of defect formation [79].

Besides the enhanced interbilayer repulsion, there should be an additional electrostatic contribution to the free energy of defect formation from the *in-plane* repulsion across the aqueous regions within the bilayer. Since the in-plane surface separation h_w is not much different from the interplane surface separation $2b_w$, we expect this contribution to be considerably smaller than the curvature energy. (For all three defect geometries, h_w exceeds 20 Å.)

The experimental value for the elasticity κ, deduced from x-ray-scattering studies of fluctuations in the long-range translational order in the L_α phase [78], also includes an electrostatic contribution κ_{es}. Recent theoretical work [63,64] shows that κ_{es} scales as b_w/λ_B with the proportionality constant estimated [64] to be $0.06k_BT$ (for the monolayer elasticity). While the electrostatic contribution may dominate κ for dilute L_α samples, it thus appears to be negligible for our sample ($\kappa_{es} \approx 0.3k_BT \ll \kappa \approx 10k_BT$). We note, however, that since the electrostatic repulsion in the present salt-free system is long ranged, its curvature dependence cannot be fully described by a renormalized elasticity. Hence, the in-plane repulsion is not properly accounted for by the curvature energy.

In the preceding discussion of defect energetics, we assumed that defects were formed without altering the bilayer thickness $2b_0$. While a relatively small change in b_0 would not significantly affect our conclusions about the curvature energy and the interbilayer repulsion, it might produce a direct chain packing contribution to the free energy of defect formation. However, mean-field calculations by Gruen [82] suggest that this contribution is modest: the free-energy cost of varying b_0 within a range of 3

Å around the optimum is less than $0.1k_BT$ for a C_{11} chain.

X. SPIN RELAXATION AS A CURVATURE PROBE

As noted in the Introduction, a variety of experimental techniques have been used to study structural defects in L_α phases. The spin-relaxation technique used here has several important advantages. First, it is a *curvature probe:* the existence of curved interfaces is unambiguously established by the observation of a relaxation anisotropy. Second, it directly reflects the *length scale* associated with the curvature defects: the observation of a frequency dependence (in the nonadiabatic spectral densities) clearly excludes bilayer undulations and textural defects as the origin of interface curvature. Third, the *model-independent information content* exceeds that available by other methods: apart from the quadrupole splitting, there are six independent nonadiabatic crystal-frame spectral densities (and more if the magnetic-field strength is varied) that reflect the microstructure. Fourth, the results can be checked by studying the relaxation of different interfacially confined nuclear species. Besides the sodium counterions used here, the present system could be studied via the ^2H relaxation of selectively deuterated SDS or decanol.

Previously, only *static* magnetic resonance (NMR and ESR) experiments have been used to study bilayer defects. Although the quadrupole splitting (or, more generally, the line shape) is a probe of interface curvature, this information is not directly accessible since the residual quadrupole coupling constant is usually unknown [cf. (4.8)]. Furthermore, the quadrupole splitting cannot distinguish between intrinsic structural defects and larger-scale textural defects.

In analyzing the relaxation data, our aim has been to proceed as far as possible without introducing specific (geometric) model assumptions. Assuming a Lorentzian shape for the crystal-frame spectral density functions, we could thus determine the two geometric quantities σ_2 and σ_4 as well as two or three correlation times. The availability of two independent geometrical quantities, which is a consequence of the fourth-rank tensorial character of the spin-relaxation observables [46,47], severely restricts the range of compatible microstructures and, in the case of pores, allows us to determine separately the relative size and density of defects.

Except for the case of oblate spheroids, we have not made use of the full information content of the crystal-frame spectral densities. More severe constraints on the microstructure could be obtained by calculating the spectral densities for various interface geometries; however, the only nontrivial geometries for which such calculations have so far been carried out are the prolate and oblate spheroids [54] and the truncated catenoid (without adjoining planar surface) [65]. At present, we can only say that the correlation times of ~ 2 ns (Tables IV and VII) deduced here (within the Lorentzian approximation) are of the expected magnitude. For the Na^+ counterions in the nearby H_α phase, composed of circular cylinders, we obtained [43] a correlation time of 2.5 ± 0.2 ns. Comparing this to the result $\tau_A=\tau_B=2.3\pm0.8$ ns for the elliptic ribbon, we note that although the cross section is noncircular, b is smaller than in the H_α phase. The Lorentzian approximation is admittedly a weakness in our analysis, although, we believe, not a serious one. It could be checked by performing accurate field-variable relaxation measurements.

Another potential source of systematic error in our analysis is the assumption of a laterally uniform counterion distribution, which is required in order to reduce the quantities σ_2 and σ_4 to geometry. In the presence of defects, the L_α phase has a larger surface-to-volume ratio than would otherwise be the case. For example, from the results in Table V we can calculate that hemitoroidal pores increase the total surface area by $\sim 40\%$. This excess surface area is certainly not uniformly distributed. Electrostatic considerations suggest a higher proportion of SDS anions (and hence of counterions) in regions of positive curvature [83], and this has also been inferred experimentally [35,84,85]. Since chain packing requirements tend to reduce the charge density in curved regions, the net effect on the lateral counterion distribution is probably small. Furthermore, the *ratio* σ_2/σ_4 is not affected by the overall partitioning of the counterions between planar and curved interface regions. The importance of lateral inhomogeneities could be directly assessed by performing a spin-relaxation study on deuterated SDS and/or decanol.

A complication in *counterion* spin-relaxation studies of microstructure is the contribution from "radial" (normal to the interface) diffusion. (This complication does not arise for amphiphile nuclei.) As discussed in Appendix A, radial diffusion contributes mainly to the crystal-frame spectral densities with symmetry index $n=0$ and the contribution should not exceed $10\ s^{-1}$. For the pore and ribbon geometries, the effect on the derived quantities in Tables IV, VI, and VII of including this *maximal* radial-diffusion contribution is as follows: $\bar{\chi}$ is reduced by 10%, $J_{\rm loc}$ is increased by 10–20 %, σ_2/σ_4 is increased by 10%, and the correlation times are increased by 10–25 %. These effects are not sufficiently large to significantly alter our conclusions.

The analysis of the relaxation data yields, besides geometrical information, the local-motion spectral density $J_{\rm loc}$ and the magnitude of the residual quadrupole coupling constant $\bar{\chi}$. For the Na^+ counterions in the nearby H_α phase, we obtained [43] $J_{\rm loc}=29\pm3\ s^{-1}$ and $\bar{\chi}=81\pm6$ kHz. The values deduced here (Tables IV, VI, and VII) differ significantly from the H_α results, but not unexpectedly so. (The differences are reduced if we allow for a radial-diffusion contribution.) The differences are largest for the disk geometry, although the uncertainties in $J_{\rm loc}$ and $\bar{\chi}$ are large there.

As noted in Sec. IV, the three adiabatic crystal-frame spectral densities contain information about the spectrum of bilayer undulation modes. The undulation contributions can be obtained from the data in Table III by subtracting $J_{\rm loc}$ and $J_{nn}^{C,\rm def}(0)$. The latter can be calculated from (6.1) in the case of pores, while for ribbons and disks there are contributions from other slow motions (Secs.

VII and VIII). For the pore geometry, we thus obtain $J_{00}^{C,\mathrm{und}}(0)=105\pm14\ \mathrm{s}^{-1}$, $J_{11}^{C,\mathrm{und}}(0)=212\pm17\ \mathrm{s}^{-1}$ and $J_{22}^{C,\mathrm{und}}(0)=32\pm11\ \mathrm{s}^{-1}$. Theoretically, one expects [45] for a uniaxial phase $J_{00}^{C,\mathrm{und}}(0)=3J_{22}^{C,\mathrm{und}}(0)<J_{11}^{C,\mathrm{und}}(0)$.

ACKNOWLEDGMENTS

We are indebted to Dr. Krister Fontell for performing the x-ray-diffraction experiment. This work was supported by grants from the Swedish Natural Science Research Council and the Swedish Research Council for Engineering Sciences.

APPENDIX A: SPIN RELAXATION BY COUNTERION DIFFUSION ALONG THE BILAYER NORMAL

In a classical lamellar phase, counterion diffusion induces spin relaxation by modulating the *magnitude* of the local QCC χ_{loc} established by the local motions. Since the classical bilayer is laterally homogeneous (on length scales larger than a few angstroms), $\chi_{\mathrm{loc}}(z)$ depends only on the distance z of the counterion from the charged bilayer surface, i.e., only diffusion along the bilayer normal can induce spin relaxation. Furthermore, since the classical bilayer is planar, the local EFG (averaged by the local motions) must be uniaxial. Counterion diffusion can therefore contribute only to the crystal-frame spectral density function with symmetry index $n=0$ [59]. Since the local EFG is short-ranged, being determined essentially by the surface-induced asymmetry in the hydration shell of the counterion and by (anisotropically distributed) ionic species in the immediate vicinity of the reference counterion [58], the components of the local EFG tensor should vanish outside an interfacial layer of thickness δ of a few angstroms. Accordingly, we model the local QCC $\chi_{\mathrm{loc}}(z)$ as a step function, taking the value χ_{loc} in the interfacial region $(0<z<\delta)$ and vanishing elsewhere $(\delta<z<b_w)$.

The contribution from "radial" (along the bilayer normal) counterion diffusion to the crystal-frame spectral densities $J_{00}^{C}(k\omega_L)$ then takes the form [59]

$$J_{\mathrm{rad}}^{C}(k\omega_L)=\pi^2\chi_{\mathrm{loc}}^2P(1-P)\int_0^\infty dt\,\cos(k\omega_L t)g_{\mathrm{rad}}(t)\ , \tag{A1}$$

where the numerical prefactor pertains to a spin-$\frac{3}{2}$ nucleus such as ^{23}Na. The reduced time correlation function in (A1), defined so that $g_{\mathrm{rad}}(0)=1$ and $g_{\mathrm{rad}}(\infty)=0$, can be expressed as [59]

$$g_{\mathrm{rad}}(t)=\frac{1}{P(1-P)}\int_0^\delta dz_0 f(z_0)\times\int_0^\delta dz[f(z,t|z_0)-f(z)]\ , \tag{A2}$$

where $f(z,t|z_0)$ is the counterion diffusion propagator and $f(z)=f(z,t\to\infty|z_0)$ is the equilibrium distribution. In (A1) and (A2), P is the fraction counterions in the interfacial layer (where the local QCC is nonzero), i.e.,

$$P=\int_0^\delta dz\,f(z)\ . \tag{A3}$$

The propagator satisfies the Smoluchowski diffusion equation [86–88]

$$\frac{\partial}{\partial t}f(z,t|z_0)=\frac{\partial}{\partial z}\left\{D(z)f(z)\frac{\partial}{\partial z}[f(z,t|z_0)/f(z)]\right\}\ , \tag{A4}$$

where $D(z)$ is the (possibly nonuniform) counterion diffusion coefficient. The partial differential equation (A4) should be solved subject to the initial condition $f(z,0|z_0)=\delta(z-z_0)$ and reflecting boundary conditions at the bilayer surface $(z=0)$ and at the midplane $(z=b_w)$ of the aqueous region, i.e., $\partial[f(z,t|z_0)/f(z)]/\partial z=0$ at $z=0$ and $z=b_w$.

The equilibrium distribution $f(z)$ is related to the potential of mean force $w(z)$ (in units of k_BT) through

$$f(z)=\exp[-w(z)]\Big/\int_0^{b_w}dz\,\exp[-w(z)]\ . \tag{A5}$$

If the counterions are modeled as point charges immersed in a dielectric continuum and the balancing interfacial charge is represented by a uniform surface charge density σ, and if ion-ion correlations are neglected [89], $w(z)$ is simply the (reduced) mean electrostatic potential obtained by solving the nonlinear Poisson-Boltzmann equation in the lamellar aqueous region [90],

$$w(z)=w(b_w)+2\ln\{\cos[(b_w-z)/\lambda_D]\}\ . \tag{A6}$$

The counterion Debye length λ_D, which always exceeds $2b_w/\pi$, is obtained from the transcendental equation [90],

$$(b_w/\lambda_D)\tan(b_w/\lambda_D)=b_w/\lambda_{\mathrm{GC}}\ , \tag{A7}$$

with the Gouy-Chapman length

$$\lambda_{\mathrm{GC}}=\frac{e}{2\pi|\sigma|\lambda_B}\ , \tag{A8}$$

and the Bjerrum length

$$\lambda_B=\frac{e^2}{4\pi\epsilon_0\epsilon_r k_BT}\ . \tag{A9}$$

From (A3), (A5), and (A6) one obtains for the fraction counterions in the interfacial layer

$$P=1-\cot(b_w/\lambda_D)\tan[(b_w-\delta)/\lambda_D]\ . \tag{A10}$$

The adiabatic spectral density $J_{\mathrm{rad}}^{C}(0)$ can actually be calculated without solving the diffusion equation (A4). The exact result is [91]

$$J_{\mathrm{rad}}^{C}(0)=\pi^2\chi_{\mathrm{loc}}^2P(1-P)\tau_{\mathrm{rel}}\ , \tag{A11}$$

with the characteristic time τ_{rel} for relaxation of the counterion distribution given by

$$\tau_{\mathrm{rel}}=\frac{1-P}{P}\int_0^\delta\frac{dz}{D(z)f(z)}\left[\int_0^z dz'f(z')\right]^2+\frac{P}{1-P}\int_\delta^{b_w}\frac{dz}{D(z)f(z)}\left[\int_z^{b_w}dz'f(z')\right]^2\ . \tag{A12}$$

Using (A5), (A6), and (A12), τ_{rel} can be calculated analytically if the diffusion coefficient is uniform in each region

[87]. (Since the resulting expression is rather long, we do not reproduce it here.)

The Poisson-Boltzmann potential (A6) is one of the few cases for which the Smoluchowski diffusion equation (A4) admits an analytical solution [87]. Inserting this solution into (A2) and carrying out the integrations in (A1) and (A2), one obtains for the case of a uniform diffusion coefficient [59]

$$J^C_{\rm rad}(k\omega_L)=\pi^2\chi^2_{\rm loc}\frac{b_w^2}{D}2q\cot(q)\sec^2(q-r)\times\sum_{m=1}^{\infty}\frac{\sin^2(m\pi r/q)}{[(m\pi)^2-q^2]^2+(k\omega_L b_w^2/D)^2}\ , \quad \text{(A13)}$$

with $q=b_w/\lambda_D$ and $r=\delta/\lambda_D$. In the adiabatic limit, the infinite series in (A13) can be summed exactly to give [59]

$$J^C_{\rm rad}(0)=\pi^2\chi^2_{\rm loc}\frac{b_w^2}{D}\frac{\cos(q)}{[2q\sin(q)\cos(q-r)]^2}\times\{\cos(q)-\cos(q-2r)+q\csc(q)[1-\cos(2r)]+2r\sin(q-2r)\}\ . \quad \text{(A14)}$$

This result is also obtained from (A11) and (A12) with $D(z)=D$.

We now use (A13) to calculate the spectral densities $J^C_{\rm rad}(k\omega_L)$ for the investigated L_α phase sample. From the sample composition, molar volumes, and x-ray repeat distance (Sec. II), we obtain (assuming classical bilayers) an aqueous lamella thickness of $2b_w=39.5$ Å and a surface charge density of $\sigma=-0.28$ C m^{-2}. For the Na^+ diffusion coefficient D, we use the bulk value [92] $D_0=1.33\times10^{-9}$ m^2 s^{-1}. The local QCC $\chi_{\rm loc}$ is obtained from the residual QCC $\bar\chi=\langle\chi_{\rm loc}(z)\rangle=P\chi_{\rm loc}$ (Sec. IV). For classical bilayers $A_Q=1$ in (4.8) so that the residual QCC is simply twice the measured quadrupole splitting $\nu_Q(\theta_{LC}=0)$, whence $\chi_{\rm loc}=64.56/P$ kHz. The thickness δ of the anisotropic interfacial layer (where $\chi_{\rm loc}$ is nonzero) should be on the order of the surfactant headgroup size. With $\delta=5$ Å and other parameters as specified above, we obtain $P=0.81$ and $J^C_{\rm rad}(0)=2.38$ s^{-1}, $J^C_{\rm rad}(\omega_L)=2.37$ s^{-1}, and $J^C_{\rm rad}(2\omega_L)=2.34$ s^{-1}. The near equality of the three spectral densities (extreme narrowing limit) is a consequence of the fast relaxation of the highly inhomogeneous counterion distribution ($\tau_{\rm res}=0.25$ ns) as compared to the Larmor frequency ($\omega_L\tau_{\rm res}=0.04\ll1$). Choosing instead $\delta=3$ Å, we obtain $P=0.71$ while the spectral densities increase by 20%.

Using (A11) and (A12), we can investigate the effect of a reduced counterion mobility in the interfacial layer. We have previously found, from spin-relaxation studies in the nearby H_α phase, that the Na^+ surface diffusion coefficient is a factor 3 smaller than D_0 [42,43]. Using this value (and $\delta=5$ Å) we obtain $J^C_{\rm rad}(0)=3.45$ s^{-1}. (Since $\omega_L\tau_{\rm res}=0.06\ll1$, we remain in the extreme narrowing limit.) As seen from Table III, even this value is within the experimental uncertainty in the CFSD's $J^C_{00}(k\omega_L)$. We thus conclude that counterion diffusion along the bilayer normal does not contribute significantly to the CFSD's *provided that the bilayers are classical.*

On the other hand, if the bilayers contain structural defects, a small but significant contribution can be expected. Essentially, the effect of structural defects is to scale up $J^C_{\rm rad}(k\omega_L)$ by a factor $(A_Q)^{-2}$, where A_Q is the geometric factor appearing in (4.8). (The effects of reduced values for b_w and σ are compensating and, hence, relatively unimportant.) These considerations suggest an upper limit of ~10 s^{-1} for $J^C_{\rm rad}(0)$.

Since the A_Q value is obtained from an analysis of the CFSD's $J^C_{nn}(k\omega_L)$ with $J^C_{\rm rad}(0)$ subtracted for $n=0$, the analysis should really be carried out iteratively until self-consistency. Using the analysis protocol of Sec. VI, we find in this way $\bar\chi=101$ kHz and $J^C_{\rm rad}(0)=8.5$ s^{-1}. It should be remembered, however, that our treatment of $J^C_{\rm rad}(k\omega_L)$ is still based on a classical bilayer geometry. (As a consequence of interface curvature, there will also be very small contributions from "radial" diffusion to the CFSD's with symmetry index $n\neq0$.) Nevertheless, it is of interest to *estimate* the effects of a maximum contribution from "radial" diffusion by repeating the analysis of Secs. VI–VIII with $J^C_{00}(k\omega_L)$ reduced by $J^C_{\rm rad}(0)=10$ s^{-1}. The results of this modified analysis are given in Sec. X.

APPENDIX B: DATA TRANSFORMATION FOR UNIAXIAL PORES

The data transformation described in Sec. VI B is a mapping from the seven-dimensional data space

$$\{\nu_0^Q,J^C_{00}(\omega_L),J^C_{00}(2\omega_L),J^C_{11}(\omega_L),J^C_{11}(2\omega_L),J^C_{22}(\omega_L),J^C_{22}(2\omega_L)\}$$

onto the seven-dimensional parameter space $\{J_{\rm loc},\bar\chi,\sigma_2,\sigma_4,\tau_0,\tau_1,\tau_2\}$. There is no *a priori* guarantee that this mapping exists. For example, if the spectral density functions $J^{C,\rm def}_{nn}(\omega)$ are distinctly non-Lorentzian, it may be impossible to map the data onto a point in the *physically admissible* region of the parameter space. Furthermore, even if the mapping exists, there is no *a priori* guarantee that it is unique, i.e., different parameter sets may correspond to the same data set. We show here that a unique mapping does in fact exist in the present case.

The data transformation is performed in the following steps.

(i) Choose a value for $J_{\rm loc}$ in the physically admissible range $[0,\min\{J^C_{nn}(k\omega_L)\}]$.

(ii) Calculate the three correlation times τ_n from (6.1) as

$$\tau_n=\frac{1}{\omega_L}\left[\frac{\alpha_n-1}{4-\alpha_n}\right]^{1/2},\quad \alpha_n=\frac{J^C_{nn}(\omega_L)-J_{\rm loc}}{J^C_{nn}(2\omega_L)-J_{\rm loc}}\ , \quad \text{(B1)}$$

(iii) Calculate the ratios $\beta_0=A_0/A_1$ and $\beta_2=A_2/A_1$ from (6.1) as

$$\beta_n=\frac{\tau_1[1+(\omega_L\tau_n)^2][J^C_{nn}(\omega_L)-J_{\rm loc}]}{\tau_n[1+(\omega_L\tau_1)^2][J^C_{11}(\omega_L)-J_{\rm loc}]}\ . \quad \text{(B2)}$$

(iv) Calculate the three amplitude factors A_n from (6.2) as

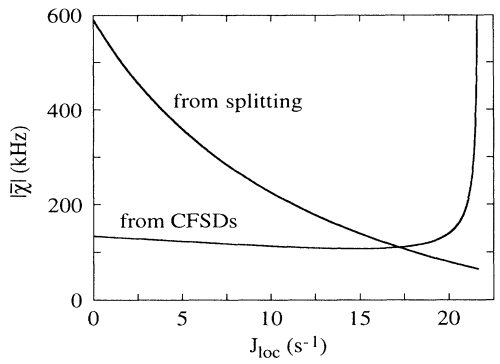

FIG. 14. Residual quadrupole coupling constant $\bar{\chi}$, calculated from the quadrupole splitting and from the nonadiabatic CFSD's, vs the local-motion spectral density J_{loc}, showing the convergence of the iterative data transformation towards a unique solution.

$$A_1=\frac{6\beta_2-\beta_0}{(1+4\beta_2)^2},\quad A_2=\beta_2 A_1,\quad A_0=\beta_0 A_1\ . \tag{B3}$$

(v) Calculate the two geometric parameters σ_m from (6.4) as

$$\sigma_2=\tfrac{2}{3}(A_1+4A_2),\quad \sigma_4=\tfrac{8}{3}A_2\ . \tag{B4}$$

(vi) Calculate the magnitude of the residual QCC from the CFSD's according to (6.1):

$$|\bar{\chi}|=\frac{1}{\pi}\left\{\frac{[1+(\omega_L\tau_0)^2][J^C_{00}(\omega_L)-J_{loc}]}{A_0\tau_0}\right\}^{1/2}\ . \tag{B5}$$

(vii) Calculate the magnitude of the residual QCC from the (non-negative) quadrupole splitting according to (4.8) and (6.9):

$$|\bar{\chi}|=\frac{2|\nu^0_Q|}{|1-\frac{3}{2}\sigma_2|}\ . \tag{B6}$$

(viii) Repeat steps (ii)–(vii) with a new value for J_{loc} until the $|\bar{\chi}|$ values calculated in steps (vi) and (vii) coincide.

Figure 14 shows the effect of varying J_{loc} on $|\bar{\chi}|$ as calculated from (B5) or (B6). Since the smallest CFSD is $J^C_{22}(2\omega_L)=28\ s^{-1}$ (Table III), we require that $0<J_{loc}<28\ s^{-1}$. However, values of $J_{loc}>21.6\ s^{-1}$ lead to physically inadmissible solutions (negative A_n). Within the physically admissible range of J_{loc} values, there is just one solution: $\{J_{loc}=17.2\ s^{-1},\ |\bar{\chi}|=110.6$ kHz$\}$. The mapping is thus unique.

[1] V. Luzzati, in *Biological Membranes,* edited by D. Chapman (Academic, New York, 1968), Vol. I, p. 71.
[2] P. Ekwall, Adv. Liq. Cryst. **1**, 1 (1975).
[3] G. J. T. Tiddy, Phys. Rep. **57**, 1 (1980).
[4] M. Kléman, C. E. Williams, M. J. Costello, and T. Gulik-Krzywicki, Philos. Mag. **35**, 33 (1977).
[5] Y. Bouligand, in *Physics of Defects,* edited by R. Balian, M. Kléman, and J. P. Poirer (North-Holland, Amsterdam, 1981), p. 667.
[6] G. J. T. Tiddy, J. B. Hayter, A. M. Hecht, and J. W. White, Ber. Bunsenges. Phys. Chem. **78**, 961 (1974).
[7] J. B. Hayter, Am. M. Hecht, J. W. White, and G. J. T. Tiddy, Faraday Disc. Chem. Soc. **57**, 130 (1974).
[8] G. J. T. Tiddy, J. Chem. Soc. Faraday Trans. I **73**, 1731 (1977).
[9] N. Boden, P. H. Jackson, K. McMullen, and M. C. Holmes, Chem. Phys. Lett. **65**, 476 (1979).
[10] N. Boden, S. A. Corne, and K. W. Jolley, Chem. Phys. Lett. **105**, 99 (1984).
[11] L. Herbst, H. Hoffmann, J. Kalus, K. Reizlein, U. Schmelzer, and K. Ibel, Ber. Bunsenges. Phys. Chem. **89**, 1050 (1985).
[12] P. J. Photinos and A. Saupe, J. Chem. Phys. **84**, 517 (1986).
[13] N. Boden, S. A. Corne, M. C. Holmes, P. H. Jackson, D. Parker, and K. W. Jolley, J. Phys. (Paris) **47**, 2135 (1986).
[14] N. Boden, S. A. Corne, and K. W. Jolley, J. Phys. Chem. **91**, 4092 (1987).
[15] M. C. Holmes, D. J. Reynolds, and N. Boden, J. Phys. Chem. **91**, 5257 (1987).
[16] G. Chidichimo, L. Coppola, C. La Mesa, G. A. Ranieri, and A. Saupe, Chem. Phys. Lett. **145**, 85 (1988).
[17] P. Kékicheff and G. J. T. Tiddy, J. Phys. Chem. **93**, 2520 (1989).
[18] P. Photinos and A. Saupe, Phys. Rev. A **41**, 954 (1990).
[19] N. Boden, J. Clements, K. W. Jolley, D. Parker, and M. H. Smith, J. Chem. Phys. **93**, 9096 (1990).
[20] P. Ukleja, G. Chidichimo, and P. Photinos, Liq. Cryst. **9**, 359 (1991).
[21] P. Photinos and A. Saupe, Phys. Rev. A **43**, 2890 (1991).
[22] N. Boden, G. R. Hedwig, M. C. Holmes, K. W. Jolley, and D. Parker, Liq. Cryst. **11**, 311 (1992).
[23] N. Boden and K. W. Jolley, Phys. Rev. A **45**, 8751 (1992).
[24] M. S. Leaver and M. C. Holmes, J. Phys. II France **3**, 105 (1993).
[25] P. J. Photinos, L. J. Yu, and A. Saupe, Mol. Cryst. Liq. Cryst. **67**, 277 (1981).
[26] M. Kuzma and A. Saupe, Mol. Cryst. Liq. Cryst. **90**, 349 (1983).
[27] P. J. Photinos and A. Saupe, J. Chem. Phys. **81**, 563 (1984).
[28] M. C. Holmes and J. Charvolin, J. Phys. Chem. **88**, 810 (1984).
[29] M. J. Sammon, J. A. N. Zasadzinski, and M. R. Kuzma, Phys. Rev. Lett. **57**, 2834 (1986).
[30] J. D. Gault, E. Kavanagh, L. A. Rodrigues, and H. Gallardo, J. Phys. Chem. **90**, 1860 (1986).
[31] M. C. Holmes, J. Charvolin, and D. J. Reynolds, Liq. Cryst. **3**, 1147 (1988).
[32] P. Kékicheff, B. Cabane, and M. Rawiso, J. Phys. Lett. (Paris) **45**, 813 (1984).
[33] P. Kékicheff and B. Cabane, Acta Crystallogr. B **44**, 395 (1988).
[34] Y. Hendrikx, J. Charvolin, P. Kékicheff, and M. Roth, Liq. Cryst. **2**, 677 (1987).
[35] Y. Hendrikx and J. Charvolin, Liq. Cryst. **11**, 677 (1992).
[36] J. M. di Meglio, M. Dvolaitzky, R. Ober, and C. Taupin, J. Phys. Lett. (Paris) **44**, 229 (1983).

[37] L. Paz, J. M. di Meglio, M. Dvolaitzky, R. Ober, and C. Taupin, J. Phys. Chem. **88**, 3415 (1984).
[38] M. Allain and J. M. di Meglio, Mol. Cryst. Liq. Cryst. **124**, 115 (1985).
[39] M. Allain, Europhys. Lett. **2**, 597 (1986).
[40] Y. Rançon and J. Charvolin, J. Phys. Chem. **92**, 6339 (1988).
[41] I. Furó, B. Halle, P-O. Quist, and T. C. Wong, J. Phys. Chem. **94**, 2600 (1990).
[42] P-O. Quist, B. Halle, and I. Furó, J. Chem. Phys. **95**, 6945 (1991).
[43] P-O. Quist, I. Blom, and B. Halle, J. Magn. Reson. **100**, 267 (1992).
[44] P-O. Quist, B. Halle, and I. Furó, J. Chem. Phys. **96**, 3875 (1992).
[45] B. Halle, P-O. Quist, and I. Furó, Phys. Rev. A **45**, 3763 (1992).
[46] S. Gustafsson and B. Halle, Mol. Phys. (to be published).
[47] B. Halle, P-O. Quist, and I. Furó, Liq. Cryst. (to be published).
[48] M. H. Cohen and F. Reif, in *Solid State Physics,* edited by H. Ehrenreich, F. Seitz, and D. Turnbull (Academic, New York, 1957), Vol. 5, p. 321.
[49] I. Furó and B. Halle, J. Chem. Phys. **91**, 42 (1989).
[50] W. H. Press, B. P. Flannery, S. A. Teukolsky, and W. T. Vetterling, *Numerical Recipes* (Cambridge University Press, Cambridge, 1986).
[51] I. Furó, B. Halle, and T. C. Wong, J. Chem. Phys. **89**, 5382 (1988).
[52] P. Ukleja, J. Pirs, and J. W. Doane, Phys. Rev. A **14**, 414 (1976).
[53] T. M. Barbara, R. R. Vold, and R. L. Vold, J. Chem. Phys. **79**, 6338 (1983).
[54] B. Halle, J. Chem. Phys. **94**, 3150 (1991).
[55] D. M. Brink and G. R. Satchler, *Angular Momentum,* 2nd ed. (Clarendon, Oxford, 1968).
[56] S. Engström, B. Jönsson, and R. W. Impey, J. Chem. Phys. **80**, 5481 (1984).
[57] J. Schnitker and A. Geiger, Z. Phys. Chem. (Munich) **155**, 29 (1987).
[58] P. Linse and B. Halle, Mol. Phys. **67**, 537 (1989).
[59] B. Halle, Mol. Phys. **53**, 1427 (1984).
[60] P. G. de Gennes, J. Phys. (Paris) Colloq. **C4**, 65 (1969).
[61] F. Brochard, J. Phys. (Paris) **34**, 411 (1973).
[62] W. Helfrich and R-M. Servuss, Nuovo Cimento **3**, 137 (1984).
[63] P. Pincus, J-F. Joanny, and D. Andelman, Europhys. Lett. **11**, 763 (1990).
[64] P. G. Higgs and J-F. Joanny, J. Phys. (Paris) **51**, 2307 (1990).
[65] B. Halle (unpublished).
[66] A. Goetz, *Introduction to Differential Geometry* (Addison Wesley, Reading, MA, 1970).
[67] C. Tanford, *The Hydrophobic Effect,* 2nd ed. (Wiley, New York, 1980).
[68] W. Helfrich, in *Physics of Defects,* edited by R. Balian, M. Kléman, and J. P. Poirer (North-Holland, Amsterdam, 1981), p. 715.
[69] A. G. Petrov and I. Bivas, Prog. Surf. Sci. **16**, 389 (1984).
[70] S. M. Gruner, J. Phys. Chem. **93**, 7562 (1989).
[71] J. Charvolin, Contemp. Phys. **31**, 1 (1990).
[72] W. Helfrich, Z. Naturforsch. **28c**, 693 (1973).
[73] A. Fogden, S. T. Hyde, and G. Lundberg, J. Chem. Soc. Faraday Trans. **87**, 949 (1991).
[74] M. D. Mitov, C. R. Acad. Bulg. Sci. **31**, 513 (1978).
[75] M. M. Kozlov, Langmuir **8**, 1541 (1992).
[76] I. Szleifer, D. Kramer, A. Ben-Shaul, W. M. Gelbart, and S. A. Safran, J. Chem. Phys. **92**, 6800 (1990).
[77] J. Ennis, J. Chem. Phys. **97**, 663 (1992).
[78] C. R. Safinya, E. B. Sirota, D. Roux, and G. S. Smith, Phys. Rev. Lett. **62**, 1134 (1989).
[79] P-O. Quist (unpublished).
[80] C. K. Bagdassarian, D. Roux, A. Ben-Shaul, and W. M. Gelbart, J. Chem. Phys. **94**, 3030 (1991).
[81] A. C. Cowley, N. L. Fuller, R. P. Rand, and V. A. Parsegian, Biochem. **17**, 3163 (1978).
[82] D. W. R. Gruen, J. Phys. Chem. **89**, 153 (1985).
[83] B. Halle, M. Landgren, and B. Jönsson, J. Phys. (Paris) **49**, 1235 (1988).
[84] Y. Hendrikx, J. Charvolin, and M. Rawiso, J. Coll. Interface Sci. **100**, 597 (1984).
[85] S. Alpérine, Y. Hendrikx, and J. Charvolin, J. Phys. (Paris) Lett. **46**, 27 (1985).
[86] M. von Smoluchowski, Ann. Phys. **48**, 1103 (1915).
[87] D. Y. C. Chan and B. Halle, Biophys. J. **46**, 387 (1984).
[88] T. Åkesson, B. Jönsson, B. Halle, and D. Y. C. Chan, Mol. Phys. **57**, 1105 (1986).
[89] B. Jönsson, H. Wennerström, and B. Halle, J. Phys. Chem. **84**, 2179 (1980).
[90] T. Ohnishi, N. Imai, and F. Oosawa, J. Phys. Soc. Jpn. **15**, 896 (1960).
[91] B. Halle, Mol. Phys. **56**, 209 (1985).
[92] R. Mills and V. M. M. Lobo, *Self-diffusion in Electrolyte Solutions* (Elsevier, Amsterdam, 1989).
[93] I. Furó (unpublished).